

An index finger exoskeleton with series elastic actuation for rehabilitation: Design, control and performance characterization

The International Journal of
Robotics Research
1–26

© The Author(s) 2015
Reprints and permissions:
sagepub.co.uk/journalsPermissions.nav
DOI: 10.1177/0278364915598388
ijr.sagepub.com



Priyanshu Agarwal¹, Jonas Fox¹, Youngmok Yun¹, Marcia K. O'Malley²
and Ashish D. Deshpande¹

Abstract

Rehabilitation of the hands is critical for the restoration of independence in activities of daily living for individuals exhibiting disabilities of the upper extremities. There is initial evidence that robotic devices with force-control-based strategies can help in effective rehabilitation of human limbs. However, to the best of our knowledge, none of the existing hand exoskeletons allow for accurate force or torque control. In this work, we present a novel index finger exoskeleton with Bowden-cable-based series elastic actuation allowing for bidirectional torque control of the device with high backdrivability and low reflected inertia. We present exoskeleton and finger joint torque controllers along with an optimization-based offline parameter estimator. Finally, we carry out tests with the developed prototype to characterize its kinematics, dynamics, and controller performance. Results show that the device preserves the characteristics of natural motion of finger and can be controlled to achieve both exoskeleton and finger joint torque control. Finally, dynamic transparency tests show that the device can be controlled to offer minimal resistance to finger motion. Beyond the present application of the device as a hand rehabilitation exoskeleton, it has the potential to be used as a haptic device for teleoperation.

Keywords

Hand exoskeleton, torque control, series elastic actuator, kinematic transparency, dynamic transparency

1. Introduction

Over 19.9 million people in the US exhibit a disability of physical function of the upper body and have difficulty lifting or grasping (Brault, 2012). Rehabilitation using robots has the potential to provide effective therapy to individuals with disabilities while also allowing for quantitative assessment of recovery. Clinical trials have shown that robot-aided hand therapy results in improved hand motor function after chronic stroke, with increased sensorimotor cortex activity for practiced tasks (Hwang et al., 2012; Takahashi et al., 2008). However, several technical challenges in areas including hand biomechanics, rehabilitation, actuators, sensors, physical human-robot interaction, and control based on the user intent (Heo et al., 2012) need to be overcome in order to design an effective, small, and lightweight robotic hand exoskeleton. Development of these exoskeletons requires physical hardware design (mechanism synthesis, human-robot interaction interface, optimal design parameters) and software-based control algorithms (subject-specific kinematics estimation, position or torque control), to ensure desirable coupled system performance.

Research over the past decade has shown initial evidence that force-control-based strategies (e.g. impedance,

admittance, assist-as-needed (Cai et al., 2006)) can be more effective for rehabilitation of both the upper (Blank et al., 2014; Colombo et al., 2005; Pehlivan et al., 2014) and lower limbs (Marchal-Crespo and Reinkensmeyer, 2009) than pure position-based control (Harwin et al., 1995). Force-control-based strategies can be designed so that an active effort is needed from the subject during therapy, which is shown to be more effective than passive motor training, even for a longer duration (Lotze et al., 2003), and is thought to be essential for provoking motor plasticity (Perez et al., 2004). On the other hand, position-control-based strategies physically guide the movement of the impaired limb to strictly follow a predefined trajectory without enabling the subject to actively participate in the task (Bernhardt et al., 2005) or allowing for any subject-specific customization of the assistance (Meng et al., 2015).

¹Mechanical Engineering Department, The University of Texas at Austin, Austin, TX, USA

²Department of Mechanical Engineering, Rice University, Houston, TX, USA

Corresponding author:

Ashish Deshpande, Mechanical Engineering Department, The University of Texas at Austin, 204 East Dean Keeton Street, Austin, TX 78712, USA.
Email: ashish@austin.utexas.edu

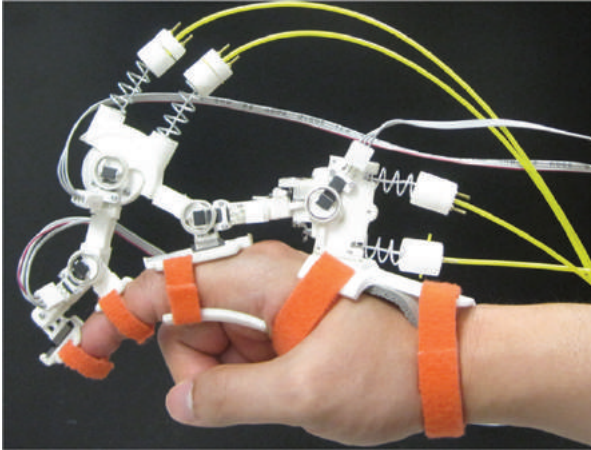


Fig. 1. Index finger exoskeleton prototype mounted on a subject's hand for experimentation.

The guidance hypothesis in motor control research suggests that such a physically guided movement may decrease motor learning for some tasks due to the reduction in burden (motor output, effort, energy consumption or attention) on the subject's motor system to discover the principles necessary to perform the task successfully (Schmidt and Bjork, 1992).

The introduction of passive compliance in the form of a Bowden-cable-based series elastic actuator (SEA) has been identified as a good force or torque source with low inertia for impedance-controlled exoskeletons, especially for the lower extremity (Veneman et al., 2006). It has been suggested for lower-extremity exoskeletons that the interaction between a therapist and a patient's limb can be simulated by applying forces corresponding to virtual springs and dampers (Vallery et al., 2008). In addition, introducing appropriate compliance in actuation can also ensure safe and comfortable interaction with the human hand. However, the role of compliance and series elastic actuation has not yet been explored in hand exoskeletons. Thus, the existing hand exoskeletons suffer from two major limitations. Firstly, none of them allow for accurate torque or impedance control at individual finger joints for effective therapy. Secondly, none of them decouples the inertia and non-linear actuator gearing effects from the human finger for kinematically and dynamically transparent (Vallery et al., 2009) interaction with the device to ensure comfort and safety.

Our goal is to design a robotic device that can provide therapeutic exercises that can lead to quicker recovery of the fingers. Toward this goal, we set the following objectives for the design of our finger-exoskeleton: (i) the device should allow for accurate and stable bidirectional torque control with high backdrivability and low reflected inertia, (ii) the design should be kinematically and dynamically compatible with the human finger and be quickly adjustable for a specific subject, and (iii) the device should be light in weight and allow for free motion of the hand with low movement resistance. We use the following design goals for the actuator for our application of hand rehabilitation: (i) a required

bidirectional peak torque of at least 0.3 Nm based on the torques applied by experienced therapists for hand rehabilitation as measured through a torque-measuring device (Ueki et al., 2012), (ii) torque bandwidth of at least 2 Hz based on the fact that the bandwidth of the human force compliance control loop is 1–2 Hz (Chan and Childress, 1990; Sheridan and Ferrell, 1974). Also, typically rehabilitation exercises for the finger are carried out at angular velocities of less than 50°/s i.e. full range of motion frequencies below 0.5 Hz (Adamovich et al., 2005; Kawasaki et al., 2006).

Physical assessment studies of hand function have shown that the loss of finger adduction or abduction motion has minimal effect on the activities of daily living (Evans, 2008). Furthermore, abduction-adduction motion is not important for achieving the critical hand functions including tip pinch, key pinch, pulp pinch, power grasp, briefcase grip, holding glass etc. and therefore is not considered during the ergonomic evaluation of biomechanical function of the hand (Lee and Jung, 2014). In addition, the index finger has limited range of motion (20 to 30 degrees) at the metacarpophalangeal (MCP) abduction-adduction joint (Anderson, 2002; Evans, 2008). Also, incorporation of an active abduction-adduction joint significantly increases the complexity of the design of our finger exoskeleton without much additional benefit. Considering all these factors, we do not include active rehabilitation of the abduction-adduction joint as the design goal for our index finger exoskeleton. The rationale behind providing passive degree of freedom (DOF) is that the device should allow for free movement at this joint while the subject performs flexion–extension motion at the other finger joints.

In this paper, we present a novel index finger exoskeleton (Figure 1) with series elastic actuation capable of achieving bidirectional and independent joint torque control at the finger joints and introduce compliance in the mechanism to make it safe and comfortable. From the robot design and controls perspective, our paper makes the following contributions: (i) presents a mechanism for a finger exoskeleton that inherently induces low joint reaction forces at the finger joints during the articulation of the finger, while providing large ranges of motion at the finger joints, (ii) implements a miniature Bowden-cable-based SEA, which is small enough to fit on a finger exoskeleton and is capable of achieving accurate torque control, (iii) presents a method of using the redundant sensor information to estimate the unknown kinematic model parameters for accurate control, and (iv) demonstrates the implementation of torque controllers for accurately applying torques both at the exoskeleton and finger joints. From the rehabilitation perspective, we present a fully developed prototype, a control system for the device, and experimental results with human subjects, that demonstrate the capabilities of the device that are critical for delivering physical therapy.

A device that directly interfaces with the human body needs testing from three different perspectives—kinematics, dynamics, and controls, and our experiments test all three

of these aspects. We characterize the performance of the device using the following experiments: (i) torque tracking performance of the SEA at different peak torque magnitudes, which showed the accuracy and fidelity of the tracking performance and a frequency analysis to verify the bandwidth of the SEA, (ii) validation of the kinematics of the device using a kinematic transparency test, active range of motion and a comparison of the finger joint angles estimated using the kinematics model and motion capture data, (iii) validation of the exoskeleton and finger joint torque tracking performance while maintaining low finger joint reaction forces at both the MCP and proximal interphalangeal (PIP) joint, and (iv) dynamic transparency tests to demonstrate the capability of the device to maintain low torques while a subject actively interacts with the device.

The rest of the paper is organized as follows. A background of the existing hand exoskeletons and their limitations are presented in Section 2. The proposed kinematic mechanism of the index finger exoskeleton, the SEA implemented for bidirectional torque control, and the details of the prototype are described in Section 3. The kinematics and statics model of the SEA and the index finger exoskeleton are presented in Section 4. The exoskeleton joint and finger joint torque controllers are explained in Section 5 along with a dynamics simulation of the controller in Section 6. Section 7 describes the implementation of the two controllers on the actual prototype and the various experiments conducted to validate the kinematic and dynamic compatibility of the device with the finger. Finally, the paper is concluded with a discussion and plans for future work.

2. Background

A number of hand exoskeletons have been designed to date, and these can be categorized into passive (with no actuators) (Brokaw et al., 2011) and active (with actuators) devices. Within the active category, devices can either provide continuous passive movement (CPM) (e.g. Waveflex CPM,¹ Kinetec Maestra Portable Hand CPM,² Ren et al. (2009)) or active assistance, where the human hand actively interacts with the device and the device reacts as per the interaction based on a feedback (e.g. position sensing) (Jones et al., 2014; Schabowsky et al., 2010; Ueki et al., 2012). There are devices that use geared servomotors either directly mounted at the exoskeleton joints (Taheri et al., 2014; Ueki et al., 2012) or connected through tendons (Jones et al., 2014). However, this makes the device bulky, restricts the hand to a stationary device and makes it difficult to achieve torque control due to losses in the gearing or routing pulleys without using explicit force feedback for controlling the device. The hand is restricted in such designs as it is attached to a stationary device on a bench top due to the fact that the forces from the transmission mechanism need to be transferred to the ground through the structure of the device.

A Bowden-cable-based mechanism allows the subject to freely orient and translate his hand within a reasonably large range for physical therapy. This is important for rehabilitation as some impairments of the upper limb make it difficult to fix the hand in certain positions. In addition, a device that would allow for free movement of the hand during operation can be used to perform activities of daily living in a rehabilitation setting both for therapy and assessment. Bowden-cable-based transmission has been employed with electric motors to make the device portable, however, these devices focus only on the position control of the digits (Cempini et al., 2014; Li et al., 2011; Wege and Hommel, 2005) and use force measurements from piezoresistive force sensors or strain gauges, either to roughly compensate for the combined resistance due to friction in the Bowden cable and moment of inertia during only finger flexion motion (no contact force information was available during extension motion) (Wang et al., 2011) or to limit the tension in the Bowden cable for safe operation (Chiri et al., 2012), or some altogether ignore the losses in the Bowden cable transmission (Sarakoglou et al., 2004). Also, experimentation with a hand exoskeleton has shown that the force measurement using force sensing resistors is inaccurate due to the nature of the sensors, inability to mount the sensors to cover the entire contact area between the device and the finger, and change in the angle of application of force to the sensor (Wege et al., 2006).

A few devices use pneumatic cylinders for actuation and estimate the force applied on the fingertips by measuring the pressure inside the cylinder (Bouzit et al., 2002; Burdea and Zhuang, 1991). However, these could not be used to control interaction force or torque at the individual phalanges or joints of the finger as their mechanism had only one DOF for each finger and is controlled by attaching the linear pneumatic actuator to only a specific phalanx. Thus, by design, any force that is applied on the distal phalanx is propagated to all the joints without any means to control it individually. In addition, the mechanism on these devices is on the palmar side, which makes it difficult to perform grasping tasks using physical objects for rehabilitation. Takagi et al. (2009) developed a system to aid in grasping, without any explicit position or force control, using air cylinders, which are pressurized or depressurized based on the output from a bending sensor. Toya et al. (2011) developed a power-assist glove that provided some assistance using pneumatic actuators by recognizing the type of grasp based on the angle information from angle sensors. Some of the devices also used EMG to control the motion of the device. These devices had a single actuator for each digit and controlled only the hand opening and closing using the EMG signal (DiCicco et al., 2004; Lucas et al., 2004; Mulas et al., 2005; Tong et al., 2010) or had multiple actuators to apply some assistive force for grasping based on EMG signal (Hasegawa et al., 2008). However, none of them could accurately control the torque applied on the finger or its position.

Hand exoskeletons have also been developed for virtual reality applications. However, these devices are designed to apply only unidirectional forces or torques to simulate contacts in a virtual environment (Gharaybeh and Burdea, 1994). Rehabilitation exoskeletons, on the other hand, are required to apply bidirectional forces on the hand during therapy. A commercially available device, CyberGrasp, is also only capable of exerting unidirectional forces to oppose the finger flexion motion with one actuated DOF for each digit (does not allow for control of torque applied at the individual finger joints) at a limited sampling rate of 90 Hz (Lii et al., 2010), which was improved to 2 kHz with an external ExHand box in Aiple and Schiele (2013).

The use of compliant foam ball exercisers and splints for hand rehabilitation has been in practice for decades (Bunnell and Boyes, 1970). Passive compliance was provided in Chiri et al. (2012) by connecting the terminal end of the Bowden cables to passive compression springs, while using a coupled actuation scheme to control all joints using a single actuator. However, remotely locating the elastic element has the drawback of reflecting the impedance of the non-linear Bowden cable drive on the human hand, thus reducing backdrivability and transparency.

3. Design

In this section, we provide the rationale behind the design of the underlying mechanism of the index finger exoskeleton, the details of the SEA configuration and the final prototype implementation.

3.1. Mechanism

Our goal is to design an index finger exoskeleton mechanism that leads to low reaction forces at the finger joints, while achieving maximum range of motion at the finger joints. Index finger consists of three joints, namely, metacarpophalangeal (MCP), proximal interphalangeal (PIP), and distal interphalangeal (DIP) (Figure 2(a)). The MCP joint has two DOFs, namely, flexion–extension (up–down motion) and abduction–adduction (sideways motion). The PIP and DIP joints have only flexion–extension motion. The three finger phalanges are called proximal, middle, and distal phalanx, respectively.

Simulation studies and experiments with existing index finger exoskeleton prototypes have shown significant loading of the finger joints when exotendons (tendons actuating the exoskeleton) are attached to links directly connected to the finger phalanges (Agarwal et al., 2013a,b; In and Cho, 2013). To avoid this loading, we first designed a mechanism in which the robotic kinematic chain is in parallel to the finger kinematic chain to ground the actuation reaction forces and form closed loops with the finger to avoid joint axes misalignment (Figure 2(a)). A study by Moran et al. (1985) has shown that mechanical stress correlates well with clinically observed patterns of frequency of degeneration and

degenerative joint disease and suggests that it is among the factors responsible for initiating and propagating joint diseases in finger joints. We introduced sliding joints as the interface between the finger phalanx and the exoskeleton link to ensure that only normal reaction forces are applied on the finger phalanges in all configurations (Figure 2(b)). Any lateral force would result in the translation of the slider until only the normal reaction force exists between the two. The normal reaction force component contributes to generating a moment at the joint while the lateral component simply loads the joint without resulting in any joint moment.

Some studies of the arm have shown that anatomical breakdown (independent motion of different joints) is better than complex arm movement for rehabilitation (Klein et al., 2012). The complexity of the task is determined by the number of anatomical joints involved in performing the task rather than the neurological effort needed. It has been shown that breaking down a simultaneous movement of the shoulder in abduction–adduction, flexion–extension, internal–external rotation and elbow in flexion–extension along sinusoidal trajectories into parts improves motor learning. A possible suggested hypothesis to explain this is that the motor system has trouble determining where the problems lie in making accurate, complex movements, and therefore breaking the movement into individual joint movements may allow for better identification and more focused practice on the key problems.

For the finger motion, breaking the simultaneous movement of both the MCP and PIP joints into motion of each joint individually could improve motor learning. In addition, a device that would enable independent motion at the MCP and PIP joint would be more versatile in rehabilitating targeted joints more effectively and assessing recovery progress. Thus, we aim for independent DOF at the finger MCP and PIP joints. We do not aim to actively actuate the DIP joint, as the PIP and DIP joints are anatomically coupled in a human hand (Levangie and Norkin, 2011). However, connecting the MCP chain with the PIP chain using a single link (L1) results in a significantly low range of motion (ROM) at the finger PIP joint due to the limited range of the available sliding length. To overcome this problem, we introduced two links (L1 and L2) connected through a revolute joint to connect the MCP chain with the PIP chain (Figure 2(c)). This resulted in one DOF in the MCP chain and a coupling between the PIP and DIP finger joints whose effects can be adjusted based on the link lengths in the two chains. However, the PIP chain has two DOF and for full actuation requires two actuators. The system can be controlled with one actuator by introducing a stiffness element in the chain (Chiri et al., 2012). However, the problem of underactuation in this design became more difficult to address as the stiffness requirement in the PIP chain varies based on the configuration of the MCP chain. We decided to remove the sliding joint in the PIP chain and fix the link to the PIP phalanx rest (exoskeleton link

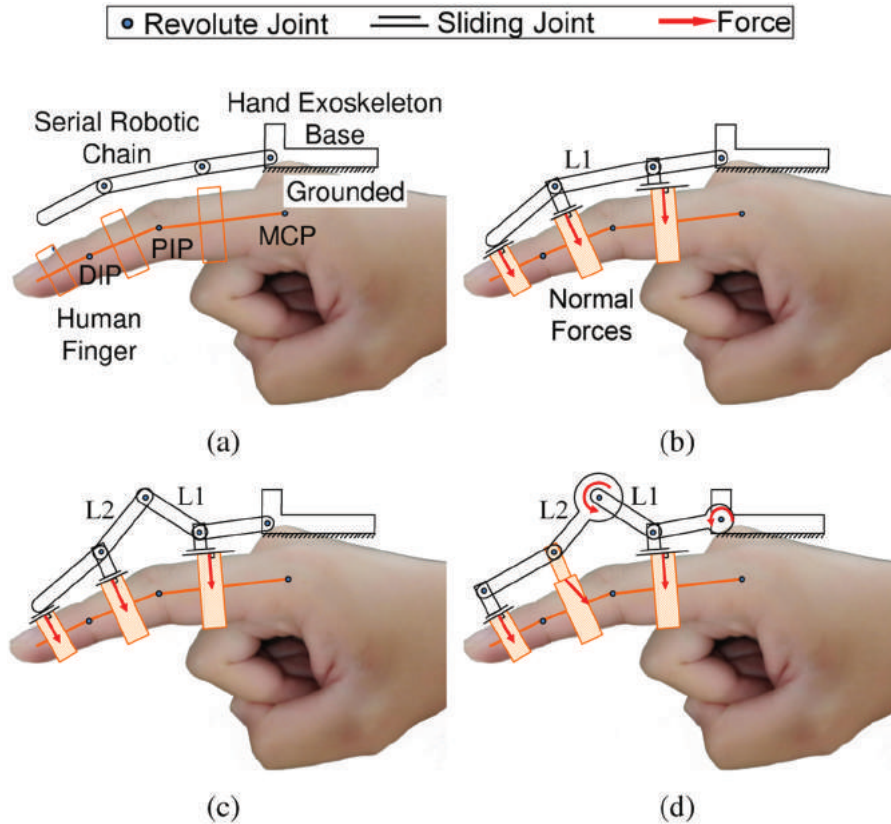


Fig. 2. Kinematic schematic of various chains in the hand exoskeleton system. (a) Kinematic chains in the system, (b) sliding joints connecting the finger and the exoskeleton kinematic chain, (c) DOF analysis of the three closed loops in the coupled system, and (d) actuated mechanism schematic. The proximal, middle, and distal chains are referred to as MCP, PIP, and DIP chains, respectively.

connected to the middle phalanx). With this configuration the PIP chain can be controlled with one actuator but also results in increased finger joint reaction forces.

In the final design (Figure 2(d)), the robotic chain was parallel to the finger, which ensured that all the actuation forces are grounded. There were three phalanx-exoskeleton closed-loop kinematic chains to avoid the joint axes misalignment problem. The MCP chain consisted of four links with three rotational and one translational joint, resulting in one DOF. The PIP chain consisted of four links with four rotational joints (assuming the first chain was fixed), resulting in one DOF. The DIP chain consisted of four links with three rotational and one translational joint leading to one DOF.

3.2. Series elastic actuation

To achieve accurate and stable force control, high backdrivability, low reflected inertia, and comfortable and safe interaction with the device, we introduced an SEA for the device. An SEA acts as a pure torque actuator and helps in reducing the undesirable forces on the finger joints. There have been a few attempts to introduce series elastic actuation in wearable exoskeletons such as for the lower extremity (Veneman et al., 2006) and upper limb (Sergi et al., 2013); however, there have been no exoskeletons for the hand that incorporate SEAs.

We use a Bowden-cable-based transmission mechanism to remotely locate the actuators and develop a miniature SEA to meet the constraints on space. However, the friction characteristics of the Bowden cable are non-linear and dependent on the cable sheath configuration, cable length, velocity, pretension, and material combination of cable and sheath (stiffness and coefficient of friction). Characterization of the Bowden cable friction as a function of the various listed factors is a part of our ongoing work (Chen et al., 2014). In order to avoid this non-linearity, we placed the stiffness element closer to the exoskeleton joint rather than the actuator. This also made the system backdrivable in addition to decoupling the motor inertia from the device. Furthermore, based on the measurement of the deflection of the stiffness element and the known stiffness, an accurate estimate of the tension in the cable can be obtained, which can then be used for accurate bidirectional torque control at the exoskeleton joint.

Directly measuring the linear displacement of the elastic element using linear potentiometers is difficult due to the limited space on a hand exoskeleton. Thus, instead of measuring the deflection of the elastic element directly, we measured the displacement of the actuator and the exoskeleton joint and estimate the deflection using the relative displacement of the two assuming stretch in the cable to be negligible. This assumption is later verified using experiments

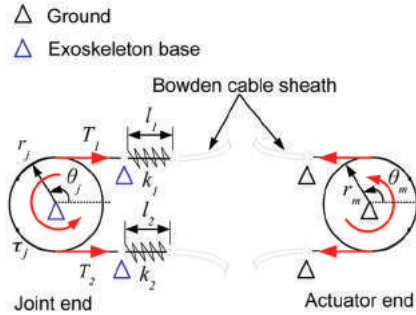


Fig. 3. Schematic of the Bowden-cable-based compression spring SEA mechanism. See Section 4.1 for definitions of the variables marked in the schematic.

carried out to quantify the torque tracking performance of the SEA. Also, the magnitude of the torque range generated at the joint for the same range of actuator displacement can be adjusted based on the magnitude of the stiffness employed. Thus, choosing the correct stiffness ensures that only appropriate forces can be applied on finger phalanges, making the device both safe and comfortable. In addition, the Bowden-cable-based actuation mechanism allows for remote actuation without constraining the subject's hand to a fixed anchor or adding any resultant forces on the exoskeleton base. There were two possible configurations of the SEA that could be implemented (Figure 3): tension and compression spring-based.

We introduced a compression spring as the elastic element of the SEA between the sheath and the exoskeleton base at the exoskeleton side (Figure 3). One end of the spring is connected to the cable sheath via clamps and the other end rested on the exoskeleton joint base. The role of the sheath in this design is to counteract the force applied by the cable and maintain zero resultant force on the device. This makes the SEA a pure torque source. Furthermore, two such compression springs are introduced, one on each side of the pulley, which makes the SEA a bidirectional torque source. In this configuration, the compression spring decreases in length as the device operates, thus avoiding any possible interference with other components during operation. Also, since one end of the compression spring rests on the exoskeleton base, there is no translation of the compression spring. This configuration reduced the space requirement on the hand exoskeleton. We therefore implemented this configuration of the SEA in our design. In a Bowden cable, the same tensile force is induced in the cable as the compressive force generated in the sheath. Thus the estimation of the compressive force using spring deflection gives a measure of the tension in the two cables and hence the torque acting at the joint.

3.3. Additive manufacturing

We chose to manufacture various components of our prototype using Selective Laser Sintering (SLS)³ with Nylon 12

(Figure 1). This additive manufacturing method allowed us to print small and intricate components, while keeping them strong and light in weight. Since size, rather than complexity, determines the cost for SLS (as opposed to complexity more than size, for conventional machining), SLS was a particularly effective manufacturing solution for our prototype. SLS was also advantageous in that it allowed us to design components that serve multiple functions (e.g. housing for the angle sensor magnets and SEA springs were integrated with the links). This helped us to reduce both the number and size of components in the design. Also, since this method allowed for quick manufacturing of the parts, it significantly reduced the development time of the prototype, leading to quick iterations of design and testing. Furthermore, the printed components were highly machinable, allowing for the post-processing needed for accurate dimensioning of critical parts and also for the required subject specific customization (if any).

3.4. Prototype

We implemented the proposed mechanism in the form of an overall design for the index finger exoskeleton (Figure 4(a)). In addition to the various joints mentioned in Section 3.1, a passive DOF for finger adduction-abduction motion in the MCP chain was also implemented in the design. The sliding and revolute joints were realized using ultra-miniature linear and rotary ball bearings. For components with significant loading, we used off-the-shelf steel parts (e.g. shafts) to reduce size and avoid excessive deformation. The entire chain is grounded on the exoskeleton base, which is attached on the wearer's hand with a velcro strap. In addition, high-density rubber foam is attached on the base for comfort to the wearer. Slots are provided on the base such that the attachment of the entire chain can be adjusted both in longitudinal and lateral directions as well as in angular position to adapt to the index finger size and natural position of the wearer.

Each link consists of two segments which can slide with respect to each other and can be locked in a specific position using a screw (Figure 4(b)). This allows for length adjustment of the links as per the requirement of the wearer's phalanx lengths. A magneto-resistive angle sensor module (KMA210, NXP Semiconductors) with a diametrically magnetized ring magnet is used as a joint angle sensor (Figure 4(c)). The ring magnet casing is built into the corresponding link, with the sensor attached to the link moving relative to the previous one. The device has five angle sensors to collect data from five joint angles, with one redundant sensor (Figure 4(a)). This redundant measurement is used to estimate the kinematic parameters of the coupled finger exoskeleton system *in situ*.

We implemented a Bowden-cable-based compression spring SEA in the prototype (Figure 4(d)). Each actuated joint consists of a pulley with a cable attached on the circumference of the pulley. The Bowden cable consists of an

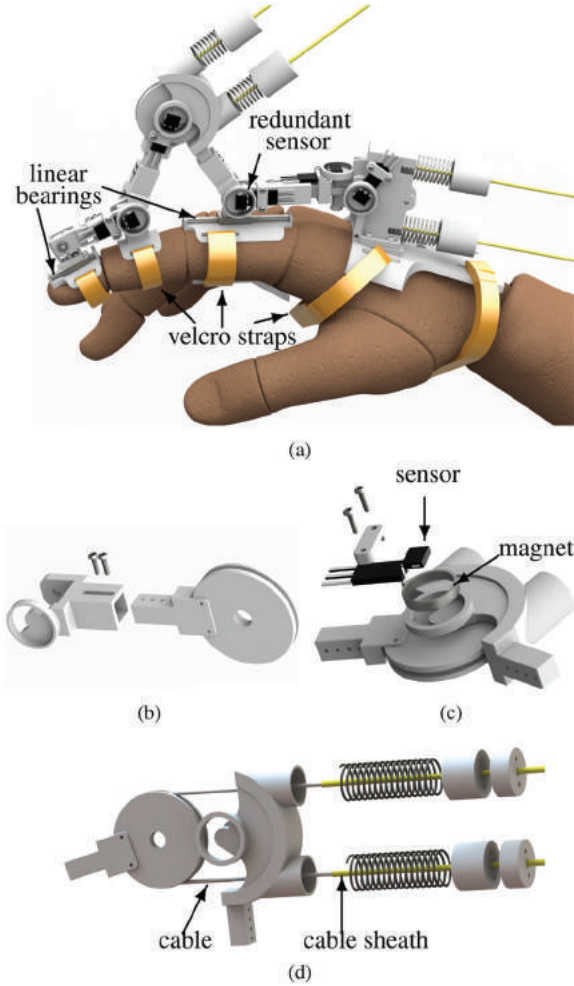


Fig. 4. CAD model of the designed index finger exoskeleton prototype. (a) Overall design of the exoskeleton, (b) adjustable link length assembly, (c) angle sensor and ring magnet assembly for joint angle sensing, and (d) Bowden-cable-based compression spring SEA design.

MFA (modified fluoroalkoxy)-coated Nylon sheath (0.125 inch outer diameter) with an FEP (fluorinated ethylene propylene)-coated stainless steel (0.026 inch diameter) wire rope to reduce the friction between the cable and the sheath. For each end of the Bowden cable connected to the joint-pulley, there is a compression spring attached to the Bowden cable sheath. When the motor actuates the joint-pulley, it first compresses the spring. The introduction of the passive series elastic element in the transmission mechanism provides a means for accurately estimating the cable tension using the joint displacement measurements obtained using the magnetic angle sensor mounted at the joint and the motor encoder. We used DC motors (RE-max 29, 22 W, Maxon Precision Motors Inc.) with planetary gearheads as the actuators for the device. The motors are mounted on a stationary platform and the Bowden cable acts as the transmission mechanism in the current design. Sufficiently long Bowden cables allow for moving the hand around without

significantly affecting the curvature of the Bowden cables. The cable tension is maintained using a cable tensioning mechanism. The mechanism consists of a sliding platform on which the motor is mounted and the position of the platform can be fixed using a lead screw mechanism that gradually builds tension in the cable.

The entire kinematic chain is actuated in the center plane of the mechanism to ensure that no sideways forces are applied on the finger while the device is actuated. Remote actuation along with SLS using Nylon 12 significantly reduces the overall weight (hand base (30 g) + finger exoskeleton (50 g) \approx 80 g) of the device compared to other exoskeletons (110 g for HANDEXOS (Chiri et al., 2012), 140 g for CAFE (Jones et al., 2014)). The design also allows for the possibility of replacement of the stiffness element (for adjusting the achievable torque range specific to a subject) without having to remove the cables.

4. System modeling

4.1. Series elastic actuator

The kinematic relationship in the system with the two springs of same effective stiffness values ($k_1 = k_2 = k$) (assuming the stretch in the cable to be negligible at the operating loads) is given by (1) (Figure 3).

$$\Delta l_1 = -\Delta l_2 = r_j(\theta_j - \theta_{j0}) - r_m\theta_m \quad (1)$$

where Δl_i is the extension in spring with length l_i . r_j and r_m are the joint and motor pulley radii, respectively. θ_j and θ_m are the joint and motor angles, respectively. θ_{j0} is the initial joint angle. The torque (τ_j) acting at the SEA joint due to the difference in the tensions (T_1 and T_2) in the two cables is given by (2).

$$\tau_j = (T_2 - T_1)r_j = 2k(r_m\theta_m - r_j(\theta_j - \theta_{j0}))r_j \quad (2)$$

4.2. Index finger exoskeleton

Control of the developed device requires good estimates of the joint angles of the wearer and the forces acting in the system. We therefore developed the kinematic and statics model of the mechanism to estimate the finger joint angles and static torques of the wearer. We assumed small abduction-adduction joint angles for the index finger and thus analyzed the mechanism for planar motion.

4.2.1. Kinematics. The loop-closure equation for the proximal (MCP) chain of the index finger exoskeleton (Figure 5) is given by (3).

$$l_{BC}e^{i\theta_1} + l_{CD}e^{i\theta_2} + x_3e^{i(\theta_4 - \pi)} = x_A + iy_A \quad (3)$$

where l_{BC} , l_{CD} are the lengths of the links BC and CD, respectively. x_3 represents the sliding length in MCP chain at a given configuration, θ 's represent the various angles (Figure 5). (x_A, y_A) represent the coordinate of the human

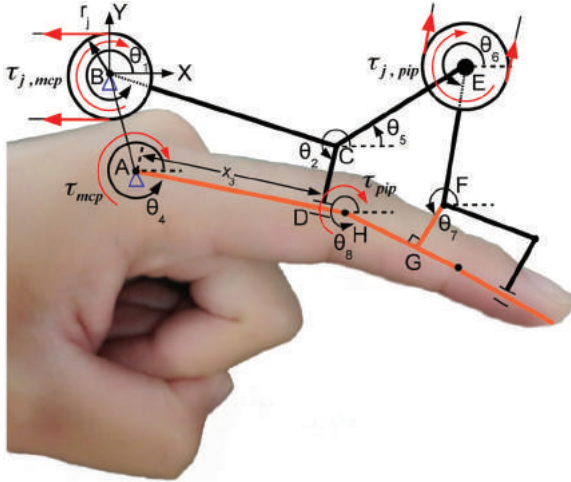


Fig. 5. Nomenclature for the kinematic model of the designed index finger exoskeleton. All angles are measured in counterclockwise direction. The arrows in red color depict forces or torques acting on the system. The arrows in black represent kinematic variables.

MCP joint (point A) in the coordinate frame located at the exoskeleton joint at B. Similarly, the loop closure equations for the middle (PIP) and distal (DIP) chains were expressed.

The forward kinematics deals with evaluating the finger MCP and PIP joint angles (θ_4 , θ_8) and the exoskeleton passive joint displacements (x_3 , θ_5) given the exoskeleton relative joint angles (θ_{1r} , θ_{6r}). The relative joint angle is the angle between the links connected at the joint as measured by the sensors mounted at the joint. Since each chain can be treated as a four-bar mechanism (by fixing the remaining DOFs), we solved for the kinematics of the system using the standard four-bar kinematics solution (Norton, 1999). In addition, we evaluated the least-squares solution for the closed-form kinematics when the system failed to evaluate the exact kinematics solution due to an error in the geometric parameters. Thus the solution can be expressed as in (4).

$$\mathbf{X} = \mathbf{X}(\Theta_r) \quad (4)$$

where $\mathbf{X} = [x_3 \ \theta_4 \ \theta_5 \ \theta_8]^T$ and $\Theta_r = [\theta_{1r} \ \theta_{6r}]^T$.

The velocity level kinematics (5) can then be obtained by differentiating the position kinematics equations for the MCP (3) and the PIP chains. We used symbolic computation in MATLAB to evaluate the Jacobian of the system (see Appendix).

$$[\dot{\mathbf{X}}]_{4 \times 1} = [\mathbf{J}(\Theta_r)]_{4 \times 2} [\dot{\Theta}_r]_{2 \times 1} \quad (5)$$

where $[\dot{\mathbf{X}}]_{4 \times 1}$ represents the velocity vector, $[\dot{\Theta}_r]_{2 \times 1}$ represents the exoskeleton joint relative velocity vector and $[\mathbf{J}(\Theta_r)]_{4 \times 2}$ represents the Jacobian of the system.

4.2.2. Statics. An experimental study has shown that the human hand dynamics is dominated by the intrinsic passive

viscoelastic torques at the finger joints (Deshpande et al., 2012). In addition, the velocities for a rehabilitation task are relatively small. Thus we consider only a statics model of the coupled finger exoskeleton system for developing a torque controller. The static forces/torques acting in the system can be related using the Jacobian as in (6).

$$\begin{bmatrix} \tau_{j,mcp} \\ \tau_{j,pip} \end{bmatrix} = \mathbf{J}(\Theta_r)^T \begin{bmatrix} f_3(=0) \\ \tau_{mcp} \\ \tau_5(=0) \\ \tau_{pip} \end{bmatrix} \quad (6)$$

where $\tau_{j,mcp}$ and $\tau_{j,pip}$ represent the torques applied at the actuated exoskeleton MCP and PIP joints, respectively, and τ_{mcp} and τ_{pip} represent the torques applied at the finger MCP and PIP joints, respectively. The force or torque acting at the linear or rotary passive joint was assumed to be zero as each joint had a bearing which made the friction at the joint small.

5. Controls

We developed two types of torque controllers for the device: exoskeleton and finger joint torque controllers. The exoskeleton joint torque controller is a basic controller implemented to test the torque control performance of the two SEAs on the device. The finger joint torque controller, on the other hand, is a more complex controller which controls the torque being applied at the individual finger joints based on a subject-specific kinematics and statics model. In addition, accurate operation of these controllers required estimation of the kinematic parameters for a specific subject. We implemented an optimization-based technique to estimate the kinematic parameters of the coupled finger exoskeleton system for a specific subject.

5.1. Exoskeleton joint torque control

The goal of this controller was to track the desired torque trajectories at the exoskeleton SEA joints (Figure 6). The output of the system was considered to be the torque generated at the exoskeleton joints through SEA as expressed in (7).

$$\hat{\mathbf{y}} = \begin{bmatrix} \tau_{j,mcp} \\ \tau_{j,pip} \end{bmatrix} = 2\mathbf{K}r_j (r_m \Theta_m - r_j(\Theta_r - \Theta_{r0})) \quad (7)$$

where

$$\mathbf{K} = \begin{bmatrix} k_{j,mcp} & 0 \\ 0 & k_{j,pip} \end{bmatrix}, \quad \Theta_m = \begin{bmatrix} \theta_{m,mcp} \\ \theta_{m,pip} \end{bmatrix}$$

$k_{j,mcp}$ and $k_{j,pip}$ represent the magnitude of the effective stiffness at the exoskeleton MCP and PIP joints, respectively, and $\theta_{m,mcp}$ and $\theta_{m,pip}$ are the MCP and PIP motor angles,

respectively. The PID controller with the corresponding feed-forward term is then given by (8).

$$\begin{aligned} \mathbf{e} &= \mathbf{y}_d - \hat{\mathbf{y}} \\ \dot{\mathbf{e}} &= \dot{\mathbf{y}}_d - \dot{\hat{\mathbf{y}}} \\ \mathbf{u} &= \frac{1}{r_m} \left(\frac{\mathbf{K}^{-1} \mathbf{y}_d}{2r_j} + r_j (\boldsymbol{\Theta}_r - \boldsymbol{\Theta}_{r0}) \right) + \mathbf{K}_p \mathbf{e} + \mathbf{K}_d \dot{\mathbf{e}} + \mathbf{K}_i \int \mathbf{e} dt \end{aligned} \quad (8)$$

where \mathbf{e} is the vector containing exoskeleton joint torque errors, \mathbf{y}_d is the vector containing the desired torque at the two exoskeleton joints and \mathbf{u} is the control input vector for the two exoskeleton joints. The gain matrices for the controller are given by

$$\mathbf{K}_p = \begin{bmatrix} k_{p,mcp} & 0 \\ 0 & k_{p,pip} \end{bmatrix}, \quad \mathbf{K}_d = \begin{bmatrix} k_{d,mcp} & 0 \\ 0 & k_{d,pip} \end{bmatrix}$$

$$\mathbf{K}_i = \begin{bmatrix} k_{i,mcp} & 0 \\ 0 & k_{i,pip} \end{bmatrix}$$

5.2. Finger joint torque control

The two actuated exoskeleton joints contributed to the torque applied on the two finger joints due to the mechanical coupling caused by the exoskeleton mechanism. The goal of this controller was to track the desired torque trajectories at the two finger joints (MCP and PIP) by applying appropriate torques through the exoskeleton SEAs (Figure 6). Since, the contribution of the inertial effects to the dynamics of the index finger exoskeleton system is small (Deshpande et al., 2012), we evaluated the output finger joint torques based on the applied SEA joint torques as given by (9).

$$\hat{\mathbf{y}} = \mathbf{J}_n^{-T} 2\mathbf{K} r_j (r_m \boldsymbol{\Theta}_m - r_j (\boldsymbol{\Theta}_r - \boldsymbol{\Theta}_{r0})) \quad (9)$$

where J_n represents the Jacobian relating the exoskeleton joint torque to the finger joint torque and is given by (10).

$$\mathbf{J}_n = \begin{bmatrix} J_{21} & J_{22} \\ J_{41} & J_{42} \end{bmatrix} \quad (10)$$

where J_{ij} represents the (i, j) th entry in the Jacobian matrix \mathbf{J} (see (5)).

The PID controller is developed considering the corresponding feed-forward term is then given by (11).

$$\begin{aligned} \tau_{fe} &= \mathbf{y}_d - \hat{\mathbf{y}} \\ \mathbf{e} &= \mathbf{J}_n^T \tau_{fe} \\ \dot{\mathbf{e}} &= (\dot{\mathbf{J}}_n^T \tau_{fe} + \mathbf{J}_n^T \dot{\tau}_{fe}) \\ \mathbf{u} &= \frac{1}{r_m} \left(\frac{\mathbf{J}_n^T \mathbf{K}^{-1} \mathbf{y}_d}{2r_j} + r_j (\boldsymbol{\Theta}_r - \boldsymbol{\Theta}_{r0}) \right) \\ &+ \mathbf{K}_p \mathbf{e} + \mathbf{K}_d \dot{\mathbf{e}} + \mathbf{K}_i \int \mathbf{e} dt \end{aligned} \quad (11)$$

where τ_{fe} is the vector containing finger torque errors, \mathbf{y}_d is the vector containing desired torque at the two finger joints,

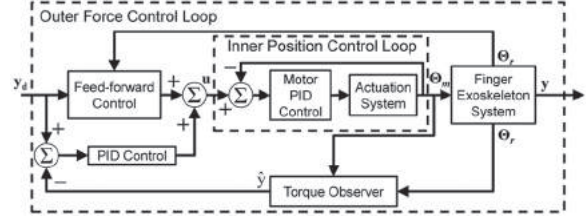


Fig. 6. The torque controllers implemented on the index finger exoskeleton. For the exoskeleton joint torque controller, the feed-forward control and torque observer refers to the exoskeleton joint torque feed-forward control and SEA-based exoskeleton joint torque estimation. For the finger joint torque controller, the feed-forward control and torque observer refers to the finger joint feed-forward torque control and finger joint torque estimation using the system statics model.

\mathbf{e} is the vector containing exoskeleton torque errors and \mathbf{u} is the desired motor position vector used as control input for the two exoskeleton joints. The derivative of the Jacobian ($\dot{\mathbf{J}}_n$), which is used to evaluate the error derivative ($\dot{\mathbf{e}}$), is computed numerically (Appendix 9).

5.3. Parameter estimation

Since the relative attachment of the exoskeleton on the wearer's hand changed the geometric parameters of the system, estimating the correct geometric parameters was essential for the controller to function. Also, it was difficult to measure the exact geometric parameters that were dependent on the hand of the wearer (Zhou et al., 2010), since the exact locations of the finger joint axes were difficult to determine. In order to deal with these problems, we used the redundant sensor data (Figure 4(a)) to estimate the uncertain geometric parameters. We collected the data from the redundant sensor for certain duration so that the full joint range of motion was traced at least once (e.g. 2 seconds for a 0.5 Hz sinusoid torque trajectory) and then used an optimization-based technique to estimate all the uncertain parameters in the system offline. We formulated the following optimization problem to estimate the parameters

$$\hat{\mathbf{P}}_{min} = \arg \min_{\hat{\mathbf{P}}} \sum_{i=1}^N (y_k - y_{m,k})^2 \quad (12)$$

where y_k and $y_{m,k}$ are the measured and the model-based redundant joint angle data, respectively. N is the number of measurements and $\mathbf{P}_k = [x_A \ y_A \ l_{BC} \ l_{CD} \ l_{AH} \ l_{FG} \ l_{GH}]^T$. The interior-point algorithm, described in Byrd et al. (1999), was used for solving the optimization problem.

6. Simulation

The proposed controller was first implemented in simulation to verify its effectiveness, before implementation on the prototype. We developed a dynamics model of the coupled finger exoskeleton system and controlled it using the

proposed finger joint torque controller. In addition, simulations helped in choosing the correct magnitude of stiffness at the two SEA joints and an appropriate Bowden cable and sheath combination for the exoskeleton.

6.1. Dynamics model

We developed a dynamics model (13) of the coupled finger exoskeleton system.

$$\mathbf{I}_j \ddot{\boldsymbol{\theta}}_j + \mathbf{B}_j \dot{\boldsymbol{\theta}}_j + \mathbf{J}_n^T \boldsymbol{\tau}_f = \boldsymbol{\tau}_j \quad (13)$$

$$\boldsymbol{\tau}_f = \begin{bmatrix} \tau_{mcp} \\ \tau_{pip} \end{bmatrix}, \quad \boldsymbol{\tau}_j = \begin{bmatrix} \tau_{j,mcp} \\ \tau_{j,pip} \end{bmatrix}$$

where I_j is the inertia matrix and B_j is the damping matrix. Since the exoskeleton links were prototyped using SLS, the link mass and inertia was low and hence we did not consider the configuration-dependent change in the inertial and Coriolis terms in the dynamics (13). We used the human finger phalanges inertia values available in the literature (Wu et al., 2008) and estimated the exoskeleton link inertia from the CAD model (Figure 4). We also assumed a linear viscous damping at the exoskeleton joints to take into account the damping due to the Bowden cable and the damping at the human joints (Barnett and Cobbold, 1968).

The motion of finger joints causes passive tissues such as tendons, ligaments, skin, and inactive muscles to be deformed. This deformation manifests in the form of a passive resistance or stiffness at the joint. A lumped passive torque model can be built by combining the contributions from all the constitutive factors. Experimental studies have shown that this passive torque at the finger joints exhibits double exponential nature (Dionysian et al., 2005; Esteki and Mansour, 1996; Kuo and Deshpande, 2012). We use this biomechanically consistent joint torque model (14) for the MCP (τ_{MCP}) and PIP (τ_{PIP}) joints (Agarwal et al., 2013a; Kuo and Deshpande, 2012) for simulation.

$$\tau_x(\theta_x) = A_x(e^{-B_x(\theta_x - E_x)} - 1) - C_x(e^{D_x(\theta_x - F_x)} - 1) \quad (14)$$

where τ_x is the passive torque offered by the joint, θ_x is the joint angle, and $A_x, B_x, C_x, D_x, E_x, F_x$ are the model coefficients. The finger joint torque controller (Section 5.2) was implemented on the device using the developed dynamics model of the coupled finger exoskeleton system to verify the effectiveness of the controller.

6.2. Simulation results

The simulation results showed that the controller developed was able to track the desired sinusoidal torque trajectories with a normalized RMS error of 1.6% (0.0032 Nm) and 9.2% (0.0037 Nm) at the finger MCP and PIP joint, respectively (Figures 7(a) and 7(b)). Also, better torque tracking was observed at the MCP joint as compared to the PIP joint as the system became more non-linear down the exoskeleton chain. This is due to the fact that both the kinematics

and the dynamics of the PIP chain is affected by the MCP chain and hence the system becomes more non-linear as one moves away from the base. The fluctuations at the peaks in the PIP joint torque did not result in large oscillations of the exoskeleton joint angles (Figure 7(c)) and were a result of the large changes in torque with small changes in angle at the extreme angles for the double exponential torque model (14). The required motor angles were well within the safe limits (Figure 7(d)) and so actuator saturation was not explicitly modeled in the controller. Also, the torque requirement for the MCP joint is higher than the PIP joint. The simulation also provided estimates of the appropriate stiffness values for the SEA springs at the MCP ($k_{j,MCP} = 2816$ N/m) and the PIP ($k_{j,PIP} = 744$ N/m) joint, which were commercially available. The stiffness values were chosen so that the requirement of the peak torque from the coupled system dynamics (13) and joint torque model (14) could be met while ensuring sufficient torque resolution under noisy joint angle sensing (motor angle >20 degrees at peak torque) along with the availability of off-the-shelf compression springs. In addition, motor angle should be in safe limits for bidirectional torque control (motor angle lies within ± 60 degrees at peak torque). Also, a smaller motor angle to achieve the peak torque allows for a higher bandwidth of the SEA. In addition, estimates of the tension in the Bowden cable also helped in choosing the appropriate Bowden cable and sheath combination.

7. Experimentation

The experiments with the SEA test rig and the exoskeleton prototype were aimed at characterizing the following: (i) the torque tracking performance and bandwidth of the SEA; (ii) the kinematic transparency of the device, i.e. how did the device affect natural motion of the finger joints; (iii) active range of motion with and without the device; (iv) validation of the kinematic model which was employed for the control of the device; (v) exoskeleton joints torque tracking performance; (vi) finger joints torque tracking performance; and (vii) dynamic transparency of the device, i.e. how did the device resist natural motion of the finger joints.

7.1. Series elastic actuator testing.

A test rig was developed for testing the stand-alone performance of the proposed SEA (Figure 8). The motor side and joint side were mounted on two different mechanical breadboards, which were separated by a meter-long Bowden cable sheath to simulate the actual scenario of the hand exoskeleton. The joint side was fixed with a six-axis load cell to measure the output joint torque and verify how close the SEA-based estimated torque values were to the measured ones. A compact magneto-resistive angle sensor similar to the one installed on the index finger exoskeleton was used to measure the joint angle and provide feedback to the

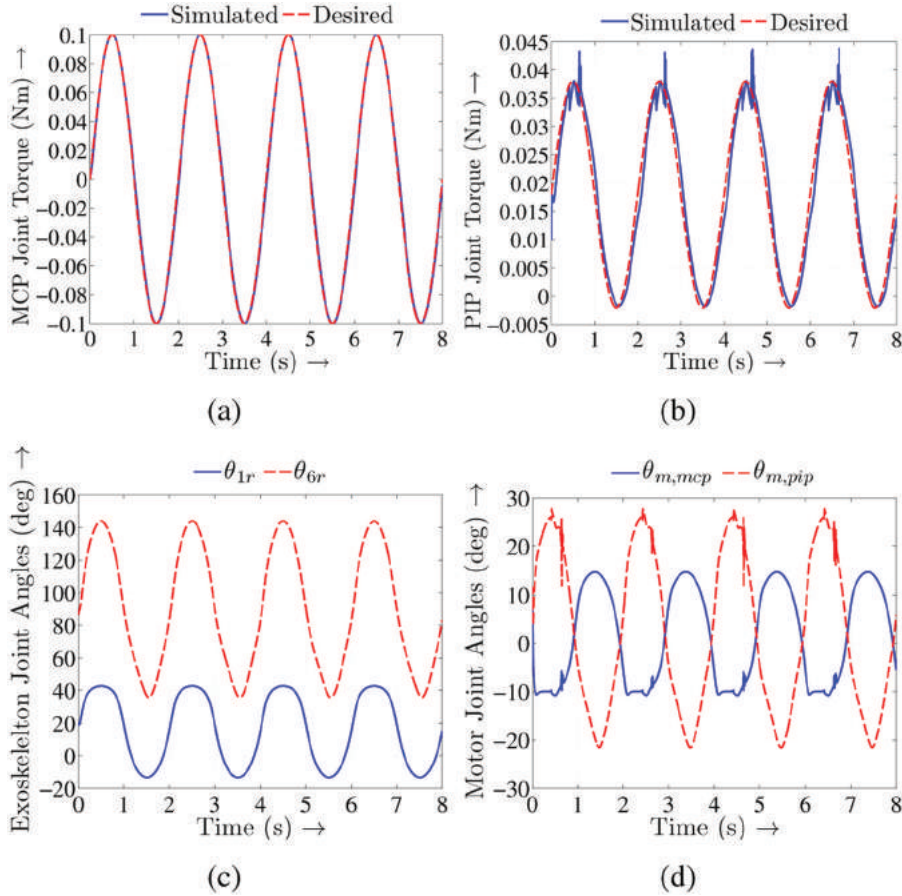


Fig. 7. The finger joints torque tracking performance for the feed-forward PID controller with sinusoidal torque input in simulation. (a) Finger MCP joint torque trajectory, (b) finger PIP joint torque trajectory, (c) exoskeleton relative joint angle trajectories at MCP (θ_{1r}) and PIP (θ_{6r}) joints, and (d) motor joint angle trajectories.

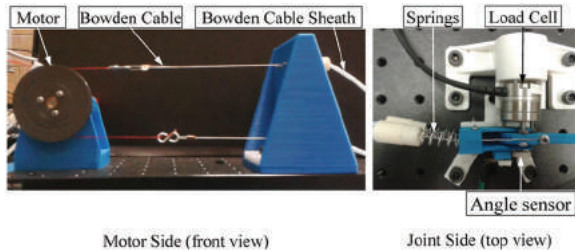


Fig. 8. The test rig developed to assess the torque tracking performance of the SEA.

torque controller to take into account the effect of sensor noise on torque control.

7.1.1. Accuracy and fidelity. The joint torque control was implemented on the test rig to verify the quality and fidelity of the torque tracking performance of the SEA. The goal was to track a sinusoidal joint torque on the SEA test rig and verify the tracking quality and fidelity of the output torque using the measurements obtained through the load cell. Torque output fidelity has been defined in the past

to quantify the distortion of the output due to the nonlinearities present in the system for SEAs (Hayward and Astley, 1996; Morrell and Salisbury, 1998; Veneman et al., 2006). We use the following measure to quantify fidelity:

$$F = \left(1 - \frac{\text{var}(y - y_d)}{\text{var}(y)}\right) \times 100\% \quad (15)$$

where F represents the force fidelity, y and y_d are the measured and the desired torque output, respectively, and $\text{var}(\cdot)$ is the variance.

7.1.2. Performance at different peak torques. An experiment was carried out to verify if the accuracy and fidelity of the SEA held at different peak torque values. We evaluated the performance of the SEA for the sinusoidal trajectories of peak torque of 0.15 Nm and 0.3 Nm at a frequency of 0.5 Hz, which would be typically encountered during our application of finger rehabilitation.

7.1.3. Torque bandwidth. Torque bandwidth is the maximum frequency at which an SEA can deliver torque. A

linear chirp signal expressed in (16) was used as the desired torque to evaluate the bandwidth of the SEA.

$$\tau_d = \tau_A \sin(2\pi(f_0 + f_1 t)t) \quad (16)$$

The magnitude ($|G_{CL}(j\omega)|$) of the frequency response of the SEAs was evaluated using the measured torque data using (17) to capture the non-linearities present in the system in frequency response.

$$|G_{CL}(j\omega)| = \frac{|\tau_{jm}(j\omega)|}{|\tau_r(j\omega)|} \quad (17)$$

where $|\tau_{jm}(j\omega)|$ and $|\tau_r(j\omega)|$, represent the single-sided amplitude spectrum of the measured and reference torque data as obtained using fast Fourier transform.

7.2. Kinematic transparency.

Since the index finger exoskeleton will be the basis for the exoskeleton modules for the other fingers, kinematic transparency tests were carried out to quantify the similarity of motion with and without the exoskeleton. Two healthy subjects (both males, ages 20–24 years) voluntarily participated in this pilot study, after they provided their informed consent (The University of Texas at Austin institutional review board study number 2013-05-0126). We used the following protocol to perform the kinematic transparency experiments. During experimentation, first the motion capture markers were placed on the various joints of the subject. The markers were placed on the side of the finger both with and without the exoskeleton to avoid any possible interference with the device and assess the performance under similar conditions (Figure 9). The subjects were asked to perform the following four different motions: (i) MCP joint articulation through full active range of motion (AROM) in flexion–extension while maintaining zero flexion angle at the PIP and DIP joints, (ii) full AROM flexion–extension at the PIP and DIP joints while maintaining zero flexion angle at the MCP joint, (iii) full AROM flexion–extension at the MCP, PIP, and DIP joints, and (iv) MCP joint full AROM while maintaining full flexion at the PIP and DIP joints. The subjects were then asked to wear the device and the link lengths were adjusted so that they can comfortably reach their full AROM with the device. The motion capture markers were again placed on the various joints and the subjects were asked to perform the four different motions with the device. The subjects were allowed to practice each motion for a certain duration (~ 2 min), after which the actual experiment was conducted. In addition, the subjects were asked to keep the motion limited to the flexion–extension plane with no abduction–adduction motion. We do not carry out motions for explicit testing of the MCP abduction–adduction motion, since in our design the joint is not actuated and its role is to allow for free finger motion sideways while performing the flexion–extension motion at the other finger joints.

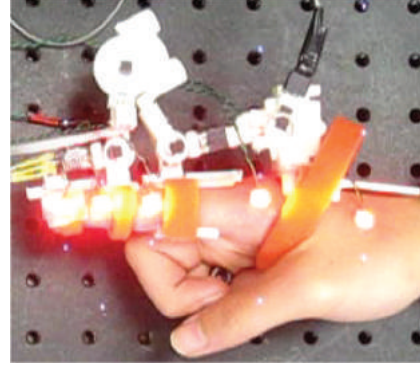


Fig. 9. The experimental setup for the hand exoskeleton system with the motion capture markers.

The experiments were performed at three different speeds—low (0.4 Hz), medium (0.8 Hz), and high (1.2 Hz). An audio cue was provided to the subjects to help them maintain the required finger frequency using a metronome. During all the experiments, the motion capture data was recorded using a motion capture system (PhaseSpace Inc.) at 480 Hz. For experiments with the exoskeleton, synchronized data from the angle sensors were also recorded at 1000 Hz. All the data acquisition subroutines were coded in C++, with the motion capture data acquisition task and the sensor data acquisition task running on two parallel threads to ensure hard real-time performance. The motion capture data was post-processed to reconstruct any missing data (Ljung, 1999), smoothed using a moving average filter, and resampled at 1/10 frequency (48 Hz) to filter out the noise. The angle sensor data was resampled at 1/10 frequency (100 Hz) to filter out the noise. Note that since these experiments were aimed at characterizing only the kinematics of device, the Bowden-cable-based SEAs were not connected during this experimentation.

7.3. Active range of motion

The subjects were asked to move their fingers at a specified frequency for the kinematic transparency tasks. However, it was difficult for the subjects to reach their full AROM while performing the task. Thus, to accurately evaluate the AROM, we separately measured the AROM for each joint with and without the device. The subjects were asked to voluntarily move their fingers to the extreme positions for each joint. An image was captured with an overhead camera to ensure that the finger plane was parallel to the image plane of the camera for accurate measurement of the angles.

7.4. Kinematic model validation

Since the data from the motion capture system and the magnetic angle sensor were collected synchronously, the former was used to validate the estimates obtained using the kinematic model with the latter. The estimates of the various kinematic parameters for the kinematic model were

obtained using the measurements obtained from an image of the coupled hand exoskeleton system. The sensor data from the MCP joint was first used to solve for the kinematics of the MCP chain. The obtained solutions along with the sensor data from the PIP chain were then used to solve for the kinematics of the PIP chain. Finally, using the PIP chain solutions and the DIP chain sensor data, the kinematics of the DIP chain was solved.

7.5. Exoskeleton joint torque tracking

The index finger exoskeleton control framework was implemented using C++ under RealTime Application Interface⁴ (RTAI) 4.0 Linux user-space to ensure hard real-time performance. The sensor data from the magneto-resistive angle sensors installed on the index finger exoskeleton was sent to the analog to digital converter (ADC) in the single-board RIO-9636 (National Instruments Inc.) data acquisition (DAQ) board equipped with a real-time 400 MHz processor and a field-programmable gate array (FPGA). The data was then filtered using a moving average filter (Smith, 2003) using the on-board FPGA. Also, the motor position was measured using the optical encoder on each motor and sent to the DAQ. The velocity estimation was then carried out both for the joint angle sensor data and the motor position data using the on-board FPGA. Next, the position and velocity data was communicated to the interface PC over Ethernet. The interface PC had a kinematics estimator, which estimated the various joint angles (for both the mechanism and the finger) in the system and communicated this information to the exoskeleton controller and a GUI (coded in Qt C++ using OpenGL) using a first-in-first-out (FIFO) queue for real-time visualization. The joint torques acting at the SEA joints were also estimated and communicated to the exoskeleton controller along with the desired torque trajectory information. The exoskeleton controller then calculated the required motor positions for both the MCP and the PIP motor. A motor angle watchdog then checked if the commanded motor positions were within the safe limits and communicated this information to the DAQ again over the Ethernet. The commanded positions were then converted to the corresponding analog signals and sent to the motor controllers (EPOS2 50/5, Maxon Precision Motors Inc.). Finally, the motor controllers executed the commanded positions using PID control. The overall higher level controller ran at 500 Hz.

The exoskeleton joint torque control was implemented on the actual prototype to test the exoskeleton joint level torque tracking performance. We used the phase and mean shifted sinusoidal trajectories as the desired torque input to the system (18).

$$\tau_{jd} = \tau_{jA} \sin(2\pi ft + \phi_j) + \tau_{j\mu} \quad (18)$$

where τ_{jd} is the desired joint torque and τ_{jA} , f , ϕ_j , and $\tau_{j\mu}$ are the amplitude, frequency, phase and mean of the sinusoidal torque trajectory. The values of various parameters in

the desired trajectories were determined experimentally for a subject by gradually increasing the desired torque amplitudes at the two exoskeleton joints within the user's comfort level. All the experiments with the actuated device were carried out with one healthy human subject who had no history of any neuromuscular disorder.

7.6. Finger joint torque tracking

The goal of the finger joint torque tracking test was to verify if the SEAs at the two exoskeleton joints can coordinate to generate desired torques at the two finger joints using the estimated system parameters (Section 5.3). We experimentally determined the parameters of the desired torque trajectories (18) for a subject by gradually increasing the desired torque amplitudes at the two finger joints within the user's comfort level. In addition, we evaluated the finger joint reaction forces both at the MCP and PIP joints by analyzing the joint reaction forces in the two four-bar chains (Norton, 1999) to ensure that the human joints were not loaded significantly.

7.7. Dynamic transparency

Finally, experiments were carried out to test dynamic transparency of the device while a subject interacts with the device. The goal was to test if the device can be controlled to offer least resistance to the finger joints. A subject wore the device and generated fast random motions. The device was controlled to render zero torque at the exoskeleton joints, which in turn should lead to zero applied torque at the finger joints.

8. Results

8.1. SEA testing

8.1.1. Accuracy and fidelity. The results from the SEA test rig show that the PID control is able to track the desired torque trajectory with a fidelity of 99.36 % (Figures 10(a) and 10(b)). The measured, best fit, desired, and estimated torques refer to the torque measured using the load cell, torque obtained by fitting the best curve to the measured torque, desired torque trajectory as available to the real-time controller, and the torque trajectory as estimated by the real-time controller using SEA-based torque evaluation. The measured, best fit, and estimated trajectories show root-mean-square errors of 0.0125 Nm (6.29%), 0.0116 Nm (5.82%) and 0.0119 Nm (5.96%), respectively, with respect to the desired torque trajectory. The measured curve shows some deviation from the estimated values, especially near the peak of the sinusoid. This is due to the error in torque estimation introduced due to the load- and configuration-dependent effective backlash (Kaneko et al., 1991) in the Bowden cable when the motor changes direction. Also, the controller was able to perform under the sensor noise as observed in the joint angle measurements (Figure 10(d)).

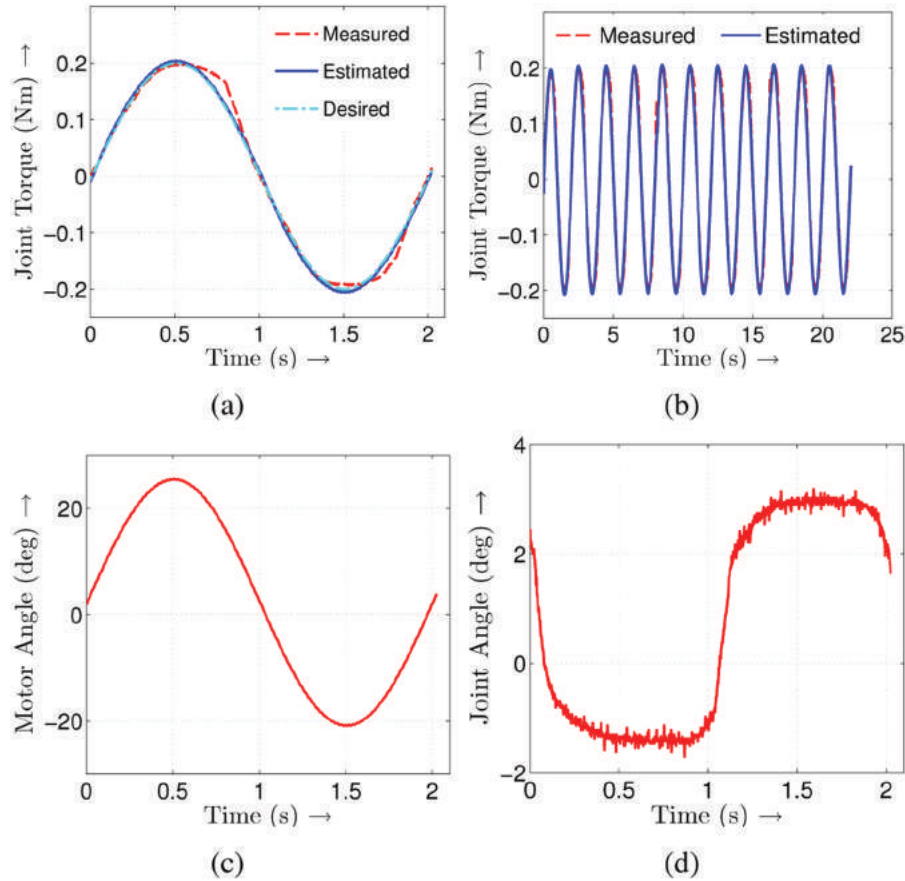


Fig. 10. The SEA joint torque tracking performance for the PID controller with sinusoidal torque input on the SEA test rig. (a) Output joint torque trajectory comparison for one cycle, (b) output joint torque trajectory tracking, (c) motor position input trajectory, and (d) joint angle trajectory.

The joint angle should ideally be zero throughout as the joint is fixed to a load cell. However, a small change in angle is observed, which is likely due to a couple of factors. First, due to the design of the exoskeleton joint, the load cell could not be directly connected on the pulley face on the test setup. Instead, three screws interfaced between the load cell and joint. When loaded, these screws deflected slightly due to their cantilever configuration. Second, these same screws interfaced with the pulley by way of through holes. These through holes were slightly larger than the screw diameter, which may have caused relative movement between the screw and pulley. Regardless, any change in the joint angle was accounted for in the estimates of the SEA torque so it did not affect our results.

8.1.2. Performance at different peak torques. The SEA was able to track the torque trajectory of 0.15 Nm and 0.3 Nm sinusoids with an RMSE of 9.28% and 11.59% and fidelity of 98.58% and 97.7%, respectively (Figure 11, Table 1). Thus the designed SEA can apply accurate and high-fidelity torques in the torque ranges required for our application of finger rehabilitation.

8.1.3. Torque bandwidth. Filtered (moving averaged) magnitude of the frequency response shows that the SEA has a bandwidth (magnitude drops below -3 dB) of over 2.5 Hz (18 rad/s), which is sufficient for our application of finger rehabilitation (Figure 12(a)). The identified second-order model showed a fitting of 85.06%. A comparison of the system response shows that the desired and measured torques have a low phase angle even at relatively higher frequencies (> 2 Hz) (Figure 12(c)). However, there is some dynamics that is not accurately captured by the second-order model, especially at the peaks, due to the non-linearities present in the system.

8.2. Kinematic transparency

For the kinematic transparency experiments, the MCP, PIP, and DIP joint angles were evaluated using the motion capture data with and without the device (Figure 13). We used Pearson's product moment correlation coefficient averaged over three repetitions to quantify the level of similarity between the joint angle trajectories with and without the exoskeleton. We use correlation as a measure of transparency instead of RMS error as it is difficult for the subject

Table 1. Joint torque root mean square error (RMSE) for the best fit, estimated and actual torque trajectories for the SEA. The percent error represents the percentage of RMS error with respect to the peak torque.

| Peak Torque Magnitude | Best fit | | Estimated | | Actual | | Fidelity |
|-----------------------|----------|------|-----------|-------|--------|-------|----------|
| | Nm | % | Nm | % | Nm | % | |
| 0.15 | 0.0128 | 8.76 | 0.0132 | 9.00 | 0.0136 | 9.28 | 98.58 |
| 0.30 | 0.0179 | 5.54 | 0.0379 | 11.76 | 0.0374 | 11.59 | 97.70 |

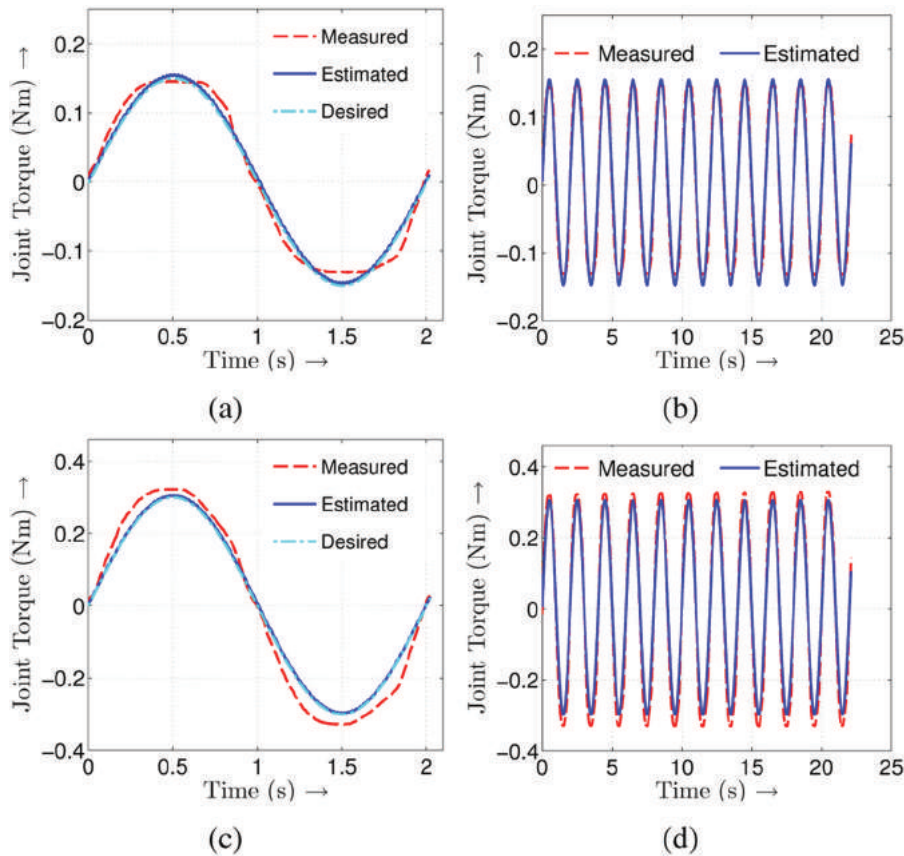


Fig. 11. The joint torque tracking performance of the SEA with sinusoidal torque input. Output joint torque trajectory comparison for peak torque magnitude of: (a), (b) 0.15 Nm and (c), (d) 0.3 Nm.

to exactly replicate the same motion over and over again with or without the device.

Results from the kinematic transparency tests showed that in general there is strong correlation between the joint angle trajectories without and with the exoskeleton (Table 2). The results for motions (ii) and (iii) showed that the exoskeleton preserved the nature of motion at the MCP, PIP, and DIP in flexion–extension and MCP in abduction–adduction (Figure 13(c), (d), (e), and (f)). For motion (i), higher PIP joint angle variation was observed with the device ($< 20^\circ$) than without it ($< 10^\circ$) (Figure 13(a) and (b)). This might be due to the coupling that exists between the exoskeleton MCP and PIP chains, which makes some motion at the PIP joint while moving the MCP joint relatively more comfortable for the subject. Also, higher motion was observed at the PIP joint for motion (iv) without the

exoskeleton ($< 30^\circ$) than with the exoskeleton ($< 10^\circ$). This shows that some deviation might be observed due to a subject’s inability to maintain constant finger joint angles for certain tasks rather than solely the kinematics of the device. In addition, some MCP abduction–adduction joint motion ($< 12^\circ$) was observed even when the subjects were instructed to maintain a constant angle at that joint, both without and with the exoskeleton. For motion (i), similar MCP abduction–adduction motion is observed without and with the device, which shows that the device allows for the natural abduction–adduction motion while performing flexion–extension motion at the other joints. Thus the overall nature of the motion at the MCP, PIP, and DIP joints is similar without with the device at all speeds. In addition, at low speeds the joint angles at the PIP joint were higher when the subject was wearing the device as compared to

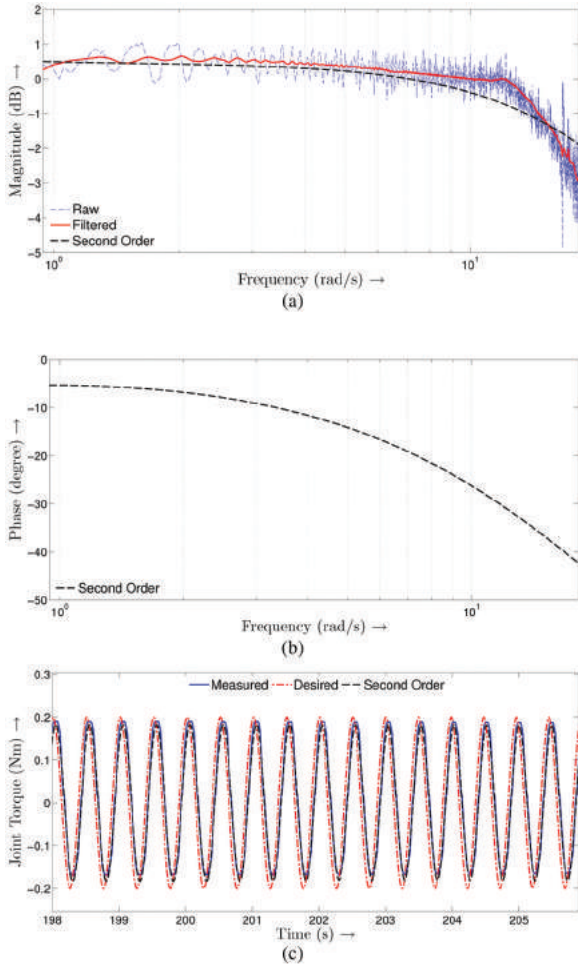


Fig. 12. Results from the frequency response analysis of the SEA: (a) magnitude from the raw measurements, filtered, and identified second-order system, (b) phase from the identified second-order system, and (c) comparison of the measured, desired, and simulated (identified second-order) system response for a portion of the chirp signal trajectory.

without the exoskeleton (Figure 13(a) and (b)). Also, the plots showed that at high speed, the angle range of the subject was significantly reduced, both without and with the exoskeleton, as the task was demanding (Figure 13(e) and (f)).

The current design with adjustable link lengths supports hand sizes with index finger lengths in the range of 60 to 80 mm, which corresponds to 95th percentile of the British adult population (both males and females) aged between 19 and 65 years (Ergonomics for Schools, 2008; Feeny, 2002). All ranges of middle and distal phalanx thickness could be accommodated as a velcro strap is used to connect the device at these phalanges. In addition, we have three different sizes for the proximal phalanx rest (link that connects to the proximal phalanx) and hand base to allow for an ergonomic fit to hands of different sizes. The design allows for quick replacement of these parts to reduce the donning time of the device.

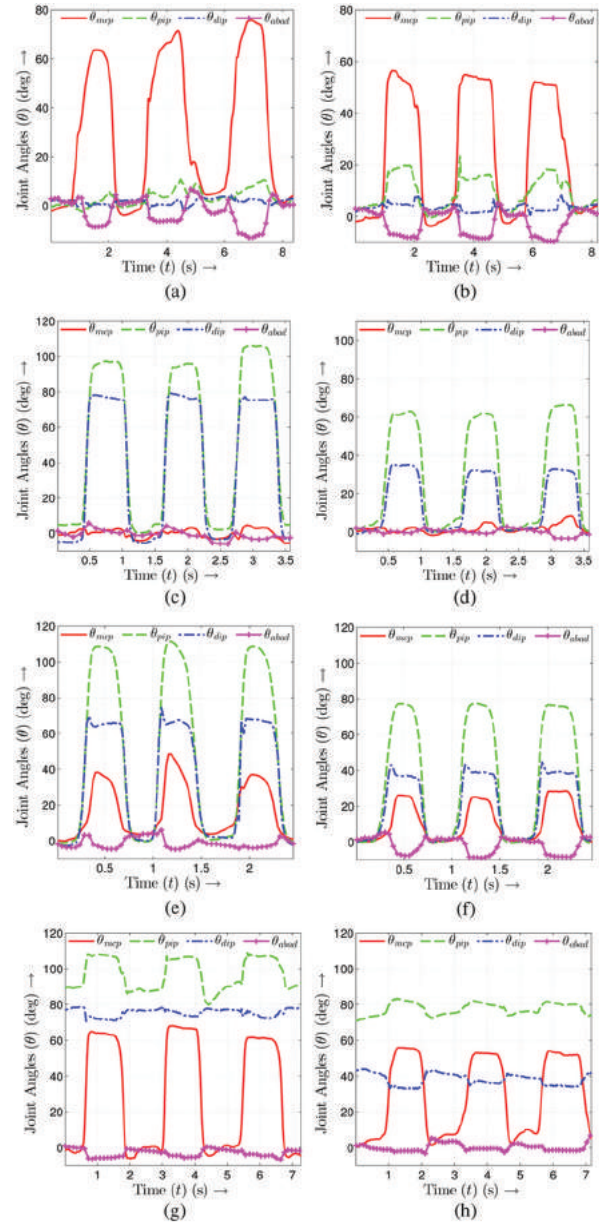


Fig. 13. Kinematic transparency results without and with the exoskeleton for one subject. The left and right columns represent the plots of the various finger joint angles without and with the hand exoskeleton for the different experiments, respectively. (a) and (b) represent the motion (i) at low speed, (c) and (d) represent the motion (ii) at medium speed, (e) and (f) represent the motion (iii) at high speed, and (g) and (h) represent the motion (iv) at low speed.

8.3. Active range of motion

The AROM with the exoskeleton was affected by the relative attachment of the device to the subjects' fingers. Table 3 presents the results of the AROM for the two subjects. Results showed that the AROM of the subject was reduced when the device is attached to the hand. The reduction in

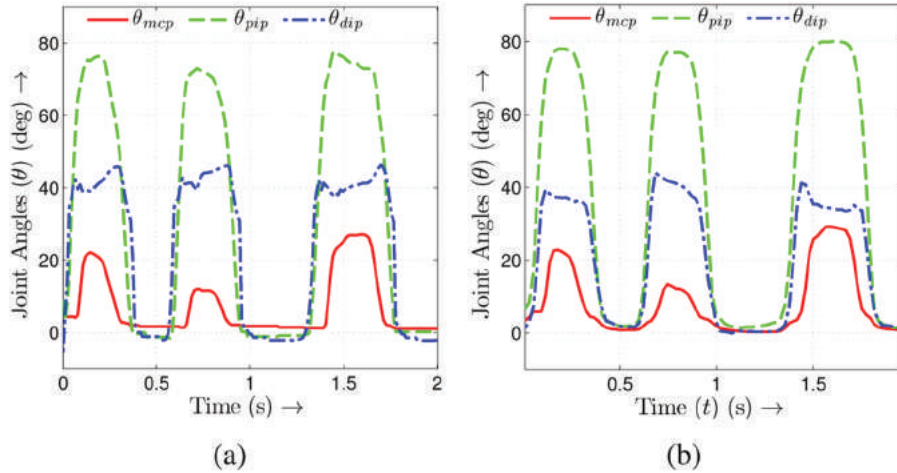


Fig. 14. A comparison of the finger joint angle estimates obtained using: (a) angle sensor data with kinematic model and (b) motion capture data.

Table 2. Pearson’s product moment correlation coefficient averaged over three repetitions as obtained from the kinematic transparency tests. The p-value was computed using a Student’s t distribution.

| Motion type | MCP | PIP | DIP |
|-------------|--------------------------|--------------------------|--------------------------|
| (i) | 0.9002 ($p < 0.01$) | – | – |
| (ii) | – | 0.9723 ($p < 0.01$) | 0.9209 ($p < 0.01$) |
| (iii) | 0.8937 ($p < 0.01$) | 0.9852 ($p < 0.01$) | 0.9892 ($p < 0.01$) |
| (iv) | 0.7888 ($p < 0.01$) | – | – |

Table 3. Active range of motion results for the different subjects without and with the index finger exoskeleton.

| Active Range of Motion | | | | | |
|------------------------|-------|---------------------|-----------|------------------|-----------|
| Subject | Joint | Without Exoskeleton | | With Exoskeleton | |
| | | Flexion | Extension | Flexion | Extension |
| Subject 1 | MCP | 94° | 5.2° | 72.1° | 2.2° |
| | PIP | 113.4° | 0.2° | 92.4° | 0° |
| | DIP | 88° | 10° | 64.13° | 8° |
| Subject 2 | MCP | 84.1° | 2.5° | 68.4° | 0.5° |
| | PIP | 125.9° | 0.5° | 89.6° | 0° |
| | DIP | 83.3° | 5.9° | 56.2° | 1.1° |

AROM was larger for PIP and DIP joints compared to the MCP joint.

8.4. Kinematic model validation

Normalized RMS differences of 5.8% (1.6878°), 7.5% (5.9485°), and 19.7% (8.6929°) are observed between the finger joint angle estimates obtained using the sensor data

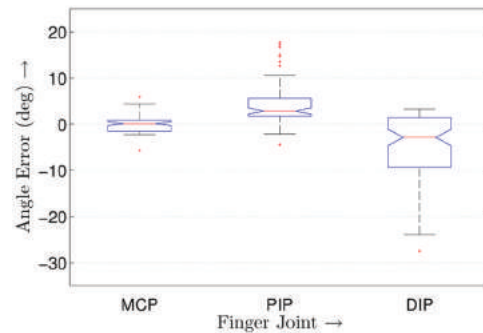


Fig. 15. Box plot of the differences between the finger joint angle estimates obtained using the sensor data with kinematic model and motion capture data. The central mark represents the median, the edges of the box are the 25th and 75th percentiles, the whiskers extend to the most extreme data points not considered outliers and the outliers are plotted individually.

with the kinematic model and the motion capture data at the MCP, PIP, and DIP joint, respectively (Figure 14(a) and (b)). A box plot of the differences also shows increasing difference in median and spread from MCP to PIP to DIP joint (Figure 15). This is because the estimates in the MCP chain affect the estimates of both the PIP and DIP chains and the estimates in the PIP chain affect the estimates of the DIP chain. This increasing model uncertainty down the exoskeleton chain leads to increased finger joint angle differences.

8.5. Exoskeleton joint torque tracking

The controller was able to track the desired torque with normalized RMS error of 2.7% (0.0061 Nm) and 14.7% (0.0064 Nm) at the exoskeleton MCP and PIP joint, respectively (Figures 16(a) and 16(b)). Limited noise was observed after filtering the exoskeleton joint angle sensor data (Figure 16(c)). However, some noise was observed

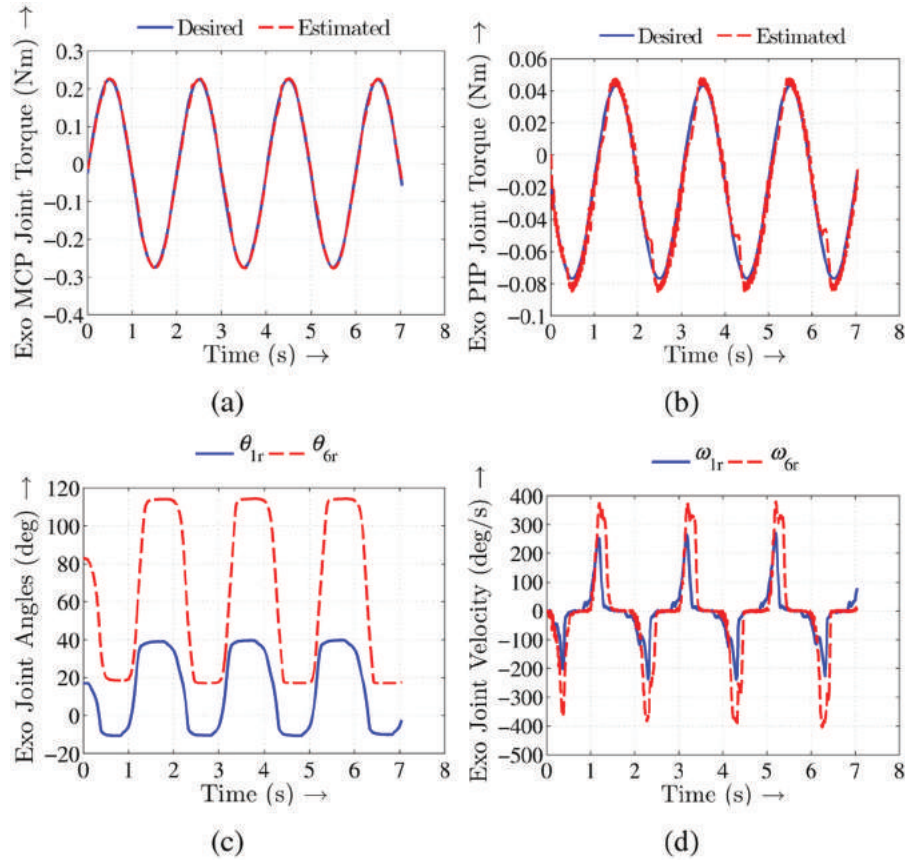


Fig. 16. The exoskeleton joints torque tracking results from the index finger exoskeleton prototype. (a) Exoskeleton MCP joint torque trajectories, (b) exoskeleton PIP joint torque trajectories, (c) exoskeleton joint angle trajectories, and (d) exoskeleton joint velocity trajectories.

in the exoskeleton joint velocity estimates due to numerical differentiation (Figure 16(d)). The residual noise in the filtered data also shows up in the estimated joint torque trajectories.

8.6. Finger joint torque tracking

The off-line parameter estimator was able to estimate the system parameters, which lie within the reasonable range based on typical hand sizes for these parameters (Table 4). The results showed that the system was able to track the desired finger torque trajectory satisfactorily well with a normalized RMS error of 1.7% (0.0041 Nm) and 3.4% (0.0012 Nm) at the finger MCP and PIP joint, respectively (Figure 17(a) and 17(b)). Also, as was observed in the simulation (Figure 7(a) and Figure 7(b)), better tracking is observed at the MCP joint as compared to the PIP joint as the system exhibits more non-linear and uncertain behavior (due to error in parameter values) down the exoskeleton chain compared to the MCP joint. The obtained Jacobian estimates were relatively noise-free (Figure 17(c)), however, some noise was observed in the Jacobian derivative estimates (Figure 17(d)) as these are obtained using the noisy velocity estimates. Also, the terms $J_{n,11}$ and $J_{n,22}$

had a much more significant contribution in the control input when compared to the other terms. However, at the derivative level the term $\dot{J}_{n,11}$ had much more significant contribution to the control input as compared to the other terms. Also, the kinematics estimator was able to estimate the various joint displacements in the coupled system using the obtained parameter estimates (Figure 17(e)). The estimates of the reaction forces at the MCP and PIP joints (Figure 17(f)) showed that the forces (< 12.5 N both at the finger MCP and PIP joints) were well below that experienced by the human finger joints while performing activities of daily living (~ 86.6 N and ~ 58.5 N at MCP and PIP joint, respectively) (Moran et al., 1985).

8.7. Dynamic transparency

The exoskeleton was able to maintain small torques both at the MCP (RMSE = 0.0029 Nm) (Figure 18(c)) and PIP joints (RMSE = 0.0092 Nm) (Figure 18(d)) throughout the arbitrary motion generated by the wearer (Figure 18(b)). Some transient residual torques were observed when the wearer performed fast movements, which settled down to zero subsequently. Residual torques generated at the exoskeleton joints were due to the error in tracking the

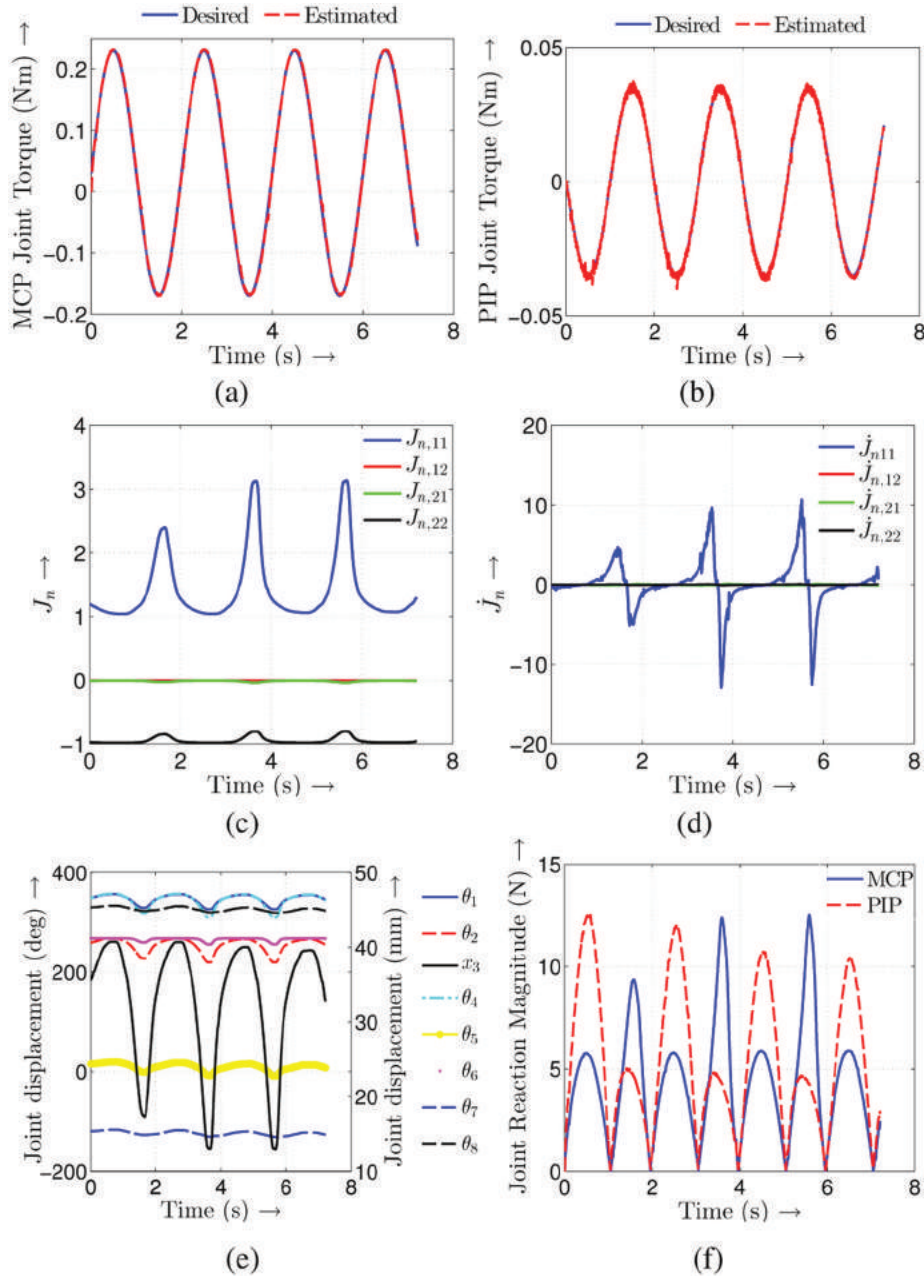


Fig. 17. The finger joints torque tracking results from the index finger exoskeleton prototype. (a) MCP finger joint torque trajectory, (b) PIP finger joint torque trajectory, (d) Jacobian estimates, (e) Jacobian derivative estimates, (c) estimated joint displacements for the various joints in the MCP and PIP chain (x_3 is plotted on the right Y-axis), and (f) finger joint reaction forces. (Best viewed in color)

desired motor joint angle trajectories (Figures 18(e) and 18(f)).

9. Discussion

We presented a novel index finger exoskeleton with Bowden-cable-based SEAs that accomplishes the stated design objectives i.e. the design should allow for accurate and bidirectional torque control with high backdrivability

and low reflected inertia, be kinematically and dynamically compatible with the human finger while being quickly adjustable to a specific subject and be light in weight while allowing for free motion of the hand with low movement resistance. Experiments showed that the device is capable of bidirectional torque control at both the exoskeleton and the finger joints. The kinematic and dynamic transparency tests showed that the device is compatible with the finger motion. Finally, the Bowden-cable-based actuation mechanism with the use of SLS for manufacturing the prototype makes the

Table 4. The offline parameter estimation results ($\hat{\mathbf{P}}$) along with the initial parameter values (\mathbf{P}_0) used for optimization.^a

| \mathbf{P} | x_A | y_A | l_{BC} | l_{CD} | l_{AH} | l_{FG} | l_{GH} |
|------------------------|--------|--------|----------|----------|----------|----------|----------|
| \mathbf{P}_0 (m) | 0.008 | -0.030 | 0.047 | 0.025 | 0.047 | 0.018 | 0.015 |
| $\hat{\mathbf{P}}$ (m) | 0.000 | -0.036 | 0.042 | 0.035 | 0.040 | 0.029 | 0.029 |
| LB (m) | -0.002 | -0.029 | 0.040 | 0.024 | 0.038 | 0.016 | 0.014 |
| UB (m) | 0.010 | -0.039 | 0.050 | 0.037 | 0.052 | 0.030 | 0.030 |

^aLB and UB represent the lower bound and upper bound, respectively, of the parameter as measured using a caliper for typical hand sizes.

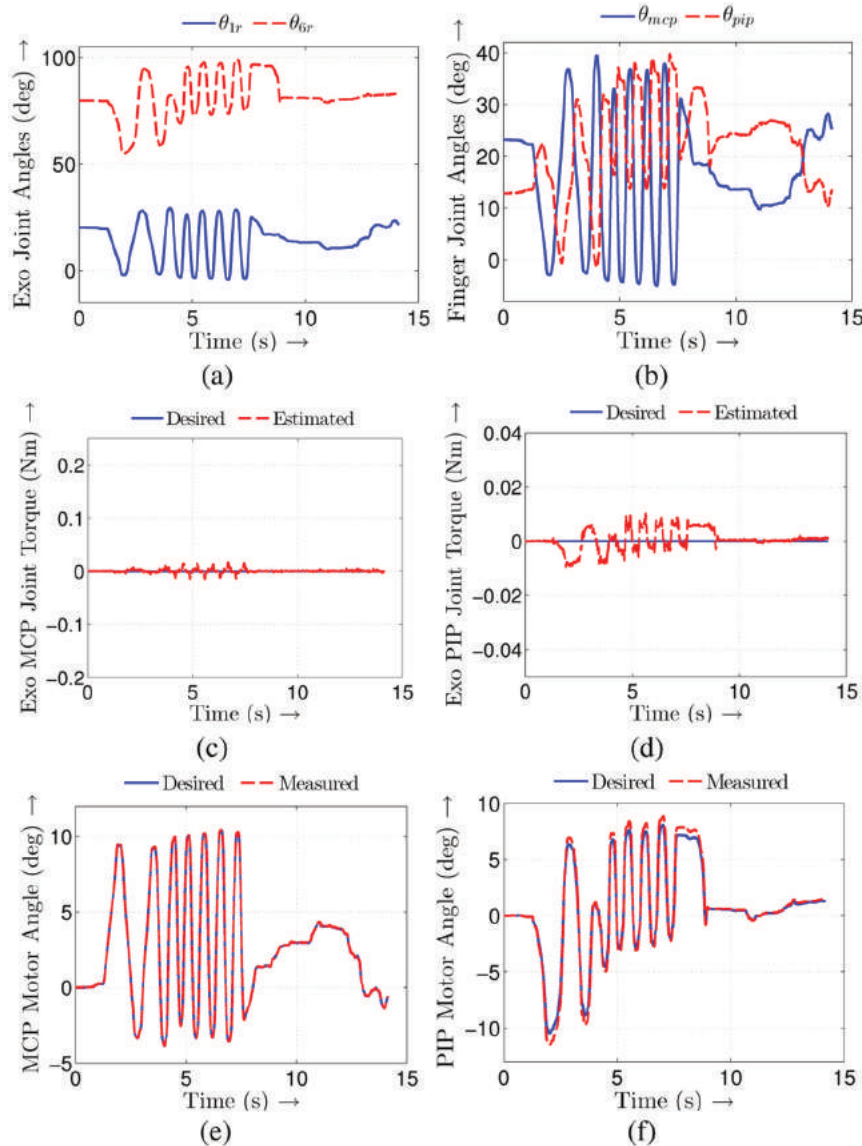


Fig. 18. The dynamic transparency test results as obtained from the index finger exoskeleton prototype. (a) Exoskeleton joint angle trajectories, (b) estimated finger joint angle trajectories, (c) exoskeleton MCP joint torque trajectories, (d) exoskeleton PIP joint torque trajectories, (e) MCP joint motor angle trajectories, and (f) PIP joint motor angle trajectories.

design light in weight (~ 80 g), while also allowing for free motion of the hand with minimal resistance.

The control experiments showed that the device actuated the finger with good bidirectional torque control. However, since it was difficult to directly measure the joint torques on the actual prototype using a load cell while a subject

was wearing the device, the estimates from the SEA were compared to the desired torque trajectory ((Figures 16(a), 16(b), 17(a), 17(b), 18(c), 18(d)). We anticipate that the actual torques would show some deviation from the desired torques, especially at the peaks, as observed on the SEA test rig (Figures 10(a), 10(b)). Also, the torques required for the

actual prototype (Figures 17(a) and 17(b)) were higher than that obtained from the simulation (Figures 7(a) and 7(b)). This is because there were several simplifications made during the simulation: (i) the finger passive joint torque model is an approximation of the torque offered by the human finger and varies among subjects, (ii) the human joint also offers some non-linear damping torque (Esteki and Mansour, 1996) which was modeled as linear, (iii) the losses due to friction at the exoskeleton joints were assumed to be negligible, and (iv) the inertial torque was not accurately modeled.

The experiments for kinematic characterization showed that the device fits well to the hands of the subjects and was easily adjustable. It was also observed that the relative attachment of the exoskeleton to the finger phalanges affected the achievable range of finger flexion–extension angle by the exoskeleton. So, by adjusting the exoskeleton attachment relative to the finger, different regions of the finger ROM can be exercised. However, there were a few limitations of the methodology used to evaluate the kinematic performance of the device. First, the motion capture data were assumed to be the ground truth for the actual motion of a subject's finger; however, there was some noise in the data, especially due to the close proximity of the markers on a subject's finger. Second, the subjects were asked to move the finger without significant adduction-abduction motion, however, some motion was observed ($< 12^\circ$) as it was difficult for the subjects to avoid it during a timed trial. Any out-of-plane rotation due to the adduction-abduction motion will result in an over-estimation of the joint angles. We are also working on optimizing the structural design of the device, including the size of the SEAs, to make it more compact. Overall the prototype manufactured using SLS was strong and light in weight. However, we plan to replace some of the small and critical load-bearing parts with metal components to ensure durability of the device. We envision that, given the pervasiveness of 3D printing technology in the future, rapid customization of the interfacing components in the design to a specific patient in a clinical setting will become a reality, thereby improving both the ergonomics and performance of the device.

Experiments showed that the robustness of the finger joint torque control is dependent on the obtained parameter estimates. In the future, we plan to implement robust control techniques (e.g. sliding mode control (Slotine and Sastry, 1983)) to accommodate for errors in the obtained parameter estimates. In addition, we plan to implement other control techniques such as impedance and assist-as-needed control (Cai et al., 2006) on the device. Furthermore, we plan to carry out human subject studies with individuals exhibiting finger pathologies to understand what control techniques can result in quicker recovery. We believe that such studies will provide us with valuable feedback, and inputs from clinicians and potential users will further help in improving the performance of the device. We also plan to carry

out a study to compare the efficacy of the device with other devices used in studies published in the literature. The device can also be geared towards rehabilitation and teleoperation applications by changing the spring stiffness at the SEA joints.

Acknowledgements

The authors thank Mark Philips, Dongyang Chen, Dan Duy Nguyen, and Prashant Rao for assisting in printing the exoskeleton parts using SLS, recommending the appropriate Bowden cables, CAD model renderings, and data acquisition setup, respectively.

Funding

This work was supported, in part, by the National Science Foundation (NSF) grants CNS-1135949 and CNS-1135916. The contents are solely the responsibility of the authors and do not necessarily represent the official views of the NSF.

Notes

1. See <http://www.remingtonmedical.com/product/detail/A1>.
2. See <http://orthoplusinc.com/index.php/products/continuous-passive-motion/kinetec-maestra-portable-hand-cpm>.
3. See http://en.wikipedia.org/wiki/Selective_laser_sintering.
4. See <https://www.rtai.org/>.

References

- Adamovich SV, Merians AS, Boian R, Lewis JA, Tremaine M, Burdea GS, Recce M and Poizner H (2005) A virtual reality-based exercise system for hand rehabilitation post-stroke. *Presence: Teleoperators and Virtual Environments* 14(2): 161–174.
- Agarwal P, Hechanova A and Deshpande A (2013a) Kinematics and dynamics of a biologically inspired index finger exoskeleton. In: *13th ASME dynamic systems and control conference*, Palo Alto, CA, USA, 21–23 October 2013. ASME.
- Agarwal P, Kuo PH, Neptune RR and Deshpande AD (2013b) A novel framework for virtual prototyping of rehabilitation exoskeletons. In: *IEEE international conference on rehabilitation robotics*, Seattle, WA, USA, 24–26 June 2013, pp. 1–6. IEEE.
- Aiple M and Schiele A (2013) Pushing the limits of the cybergrasp for haptic rendering. In: *2013 IEEE international conference on robotics and automation*, Karlsruhe, Germany, 6–10 May 2013, pp. 3541–3546. IEEE.
- Anderson J (2002) Examination and diagnosis of musculoskeletal disorders. *Australasian Radiology* 46(2): 216–217.
- Barnett C, Cobbold A (1968) Effects of age upon the mobility of human finger joints. *Annals of the Rheumatic Diseases* 27(2): 175–177.
- Bernhardt M, Frey M, Colombo G and Riener R (2005) Hybrid force-position control yields cooperative behaviour of the rehabilitation robot lokomat. In: *9th IEEE international conference on rehabilitation robotics*, Chicago, IL, USA, 28 June – 1 July 2005, pp. 536–539. IEEE.
- Blank AA, French JA, Pehlivan AU and O'Malley M (2014) Current trends in in robot-assisted upper-limb stroke rehabilitation: promoting patient engagement in therapy. *Current Physical Medicine and Rehabilitation Reports* (in press).

- Bouzit M, Burdea G, Popescu G and Boian R (2002) The Rutgers Master II-new design force-feedback glove. *IEEE/ASME Transactions on Mechatronics* 7(2): 256–263.
- Brault MW (2012) *Americans with Disabilities: 2010*. Washington, DC: US Department of Commerce, Economics and Statistics Administration, US Census Bureau.
- Brokaw EB, Black I, Holley RJ and Lum PS (2011) Hand spring operated movement enhancer (HandSOME): a portable, passive hand exoskeleton for stroke rehabilitation. *IEEE Transactions on Neural Systems and Rehabilitation Engineering* 19(4): 391–399.
- Bunnell S and Boyes JH (1970) *Bunnell's Surgery of the Hand*. Philadelphia, PA: Lippincott.
- Burdea G and Zhuang J (1991) Dextrous telerobotics with force feedback—an overview: Part 2. control and implementation. *Robotica* 9(3): 291–298.
- Byrd R, Hribar M and Nocedal J (1999) An interior point algorithm for large-scale nonlinear programming. *SIAM Journal on Optimization* 9(4): 877–900.
- Cai LL, Fong AJ, Otsoshi CK, Liang Y, Burdick JW, Roy RR and Edgerton VR (2006) Implications of assist-as-needed robotic step training after a complete spinal cord injury on intrinsic strategies of motor learning. *The Journal of Neuroscience* 26(41): 10,564–10,568.
- Cempini M, Cortese M and Vitiello N (2014) A powered finger-thumb wearable hand exoskeleton with self-aligning joint axes. *IEEE/ASME Transactions on Mechatronics* 99: 1–12.
- Chan RB and Childress DS (1990) On information transmission in human-machine systems: channel capacity and optimal filtering. *IEEE Transactions on Systems, Man and Cybernetics* 20(5): 1136–1145.
- Chen D, Yun Y and Deshpande AD (2014) Experimental characterization of bowden cable friction. In: *2014 IEEE international conference on robotics and automation*, Hong Kong, China, 31 May – 7 June 2014, pp. 5927–5933. IEEE.
- Chiri A, Vitiello N, Giovacchini F, Roccella S, Vecchi F and Carrozza MC (2012) Mechatronic design and characterization of the index finger module of a hand exoskeleton for post-stroke rehabilitation. *IEEE/ASME Transactions on Mechatronics* 17(5): 884–894.
- Colombo R, Pisano F, Micera S, Mazzone A, Delconte C, Carrozza MC, Dario P and Minuco G (2005) Robotic techniques for upper limb evaluation and rehabilitation of stroke patients. *IEEE Transactions on Neural Systems and Rehabilitation Engineering* 13(3): 311–324.
- Deshpande AD, Gialias N and Matsuoka Y (2012) Contributions of intrinsic visco-elastic torques during planar index finger and wrist movements. *IEEE Transactions on Biomedical Engineering* 59(2): 586–594.
- DiCicco M, Lucas L and Matsuoka Y (2004) Comparison of control strategies for an emg controlled orthotic exoskeleton for the hand. In: *2004 IEEE international conference on robotics and automation*, Barcelona, Spain, 18–22 April 2005, vol. 2, pp. 1622–1627. IEEE.
- Dionysian E, Kabo J, Dorey F and Meals R (2005) Proximal interphalangeal joint stiffness: measurement and analysis. *The Journal of Hand Surgery* 30(3): 573–579.
- Ergonomics for Schools (2008) Hand tools. Available at: <http://www.ergonomics4schools.com/lzone/tools.htm>.
- Esteki A and Mansour J (1996) An experimentally based nonlinear viscoelastic model of joint passive moment. *Journal of Biomechanics* 29(4): 443–450.
- Evans RC (2008) *Illustrated Orthopedic Physical Assessment*. Edinburgh: Mosby.
- Feeney R (2002) *Specific Anthropometric and Strength Data for People with Dexterity Disability*. London: Consumer and Competition Policy Directorate: Department of Trade and Industry.
- Gharaybeh MA and Burdea GC (1994) Investigation of a shape memory alloy actuator for dextrous force-feedback masters. *Advanced Robotics* 9(3): 317–329.
- Harwin WS, Rahman T and Foulds RA (1995) A review of design issues in rehabilitation robotics with reference to North American research. *IEEE Transactions on Rehabilitation Engineering* 3(1): 3–13.
- Hasegawa Y, Mikami Y, Watanabe K and Sankai Y (2008) Five-fingered assistive hand with mechanical compliance of human finger. In: *2008 IEEE international conference on robotics and automation*, Pasadena, CA, USA, 19–23 May 2008, pp. 718–724. IEEE.
- Hayward V and Astley OR (1996) Performance measures for haptic interfaces. In: *Robotics research: the 7th international symposium*. London: Springer-Verlag, pp. 195–206.
- Heo P, Gu G, Lee S, Rhee K and Kim J (2012) Current hand exoskeleton technologies for rehabilitation and assistive engineering. *International Journal of Precision Engineering and Manufacturing* 13(5): 807–824.
- Hwang CH, Seong JW and Son DS (2012) Individual finger synchronized robot-assisted hand rehabilitation in subacute to chronic stroke: a prospective randomized clinical trial of efficacy. *Clinical Rehabilitation* 26(8): 696–704.
- In H and Cho KJ (2013) Analysis of the forces on the finger joints by a joint-less wearable robotic hand, snu exoglove. In: *Converging Clinical and Engineering Research on Neurorehabilitation*, pp. 93–97.
- Jones C, Wang F, Morrison R, Sarkar N and Kamper D (2014) Design and development of the cable actuated finger exoskeleton for hand rehabilitation following stroke. *IEEE/ASME Transactions on Mechatronics* 19(1): 131–140.
- Kaneko M, Wada M, Maekawa H, Tanie K (1991) A new consideration on tendon-tension control system of robot hands. In: *1991 IEEE international conference on robotics and automation*, Sacramento, CA, USA, 9–11 April 1991, pp. 1028–1033. IEEE.
- Kawasaki H, Kimura H, Ito S, Nishimoto Y, Hayashi H and Sakaeda H (2006) Hand rehabilitation support system based on self-motion control, with a clinical case report. In: *World automation congress*, Budapest, Hungary, 24–26 July 2006, pp. 1–6. IEEE.
- Klein J, Spencer SJ and Reinkensmeyer DJ (2012) Breaking it down is better: Haptic decomposition of complex movements aids in robot-assisted motor learning. *IEEE Transactions on Neural Systems and Rehabilitation Engineering* 20(3): 268–275.
- Kuo PH and Deshpande AD (2012) Muscle-tendon units provide limited contributions to the passive stiffness of the index finger metacarpophalangeal joint. *Journal of Biomechanics* 45(15): 2531–2538.
- Lee KS and Jung MC (2014) Ergonomic evaluation of biomechanical hand function. *Safety and Health at Work* 6(1): 9–17.
- Levangie PK and Norkin CC (2011) *Joint Structure and Function: A Comprehensive Analysis*. FA Davis.
- Li J, Zheng R, Zhang Y and Yao J (2011) iHandRehab: an interactive hand exoskeleton for active and passive rehabilitation.

- In: *IEEE international conference on rehabilitation robotics*, Zurich, Switzerland, 29 June–1 July 2011. IEEE.
- Lii NY, Chen Z, Pleintinger B, Borst CH, Hirzinger G and Schiele A (2010) Toward understanding the effects of visual-and force-feedback on robotic hand grasping performance for space teleoperation. In: *23rd IEEE/RSJ international conference on intelligent robots and systems*, Taipei, Taiwan, 18–22 Oct 2010, pp. 3745–3752. IEEE.
- Ljung L (1999) Informative experiments. In: *System Identification: Theory for the User* (System Sciences Series). Englewood Cliffs, NJ: Prentice Hall Inc., pp. 361–369.
- Lotze M, Braun C, Birbaumer N, Anders S and Cohen LG (2003) Motor learning elicited by voluntary drive. *Brain* 126(4): 866–872.
- Lucas L, DiCicco M and Matsuoka Y (2004) An EMG-controlled hand exoskeleton for natural pinching. *Journal of Robotics and Mechatronics* 16: 482–488.
- Marchal-Crespo L and Reinkensmeyer DJ (2009) Review of control strategies for robotic movement training after neurologic injury. *Journal of Neuroengineering and Rehabilitation* 6(1): 20.
- Meng W, Liu Q, Zhou Z, Ai Q, Sheng B and Xie SS (2015) Recent development of mechanisms and control strategies for robot-assisted lower limb rehabilitation. *Mechatronics* (in press).
- Moran JM, Hemann JH and Greenwald AS (1985) Finger joint contact areas and pressures. *Journal of Orthopaedic Research* 3(1): 49–55.
- Morrell JB and Salisbury JK (1998) Parallel-coupled micro-macro actuators. *The International Journal of Robotics Research* 17(7): 773–791.
- Mulas M, Folgheraiter M and Gini G (2005) An EMG-controlled exoskeleton for hand rehabilitation. In: *9th IEEE international conference on rehabilitation robotics*, Chicago, IL, USA, 28 June–1 July 2005, pp. 371–374. IEEE.
- Norton RL (1999) *Design of Machinery: An Introduction to the Synthesis and Analysis of Mechanisms and Machines*. London: WCB McGraw-Hill.
- Pehlivan A, Sergi F and O'Malley M (2014) A subject-adaptive controller for wrist robotic rehabilitation. *IEEE/ASME Transactions on Mechatronics* 99: 1–13.
- Perez MA, Lungholt BK, Nyborg K and Nielsen JB (2004) Motor skill training induces changes in the excitability of the leg cortical area in healthy humans. *Experimental Brain Research* 159(2): 197–205.
- Ren Y, Park HS and Zhang LQ (2009) Developing a whole-arm exoskeleton robot with hand opening and closing mechanism for upper limb stroke rehabilitation. In: *11th IEEE international conference on rehabilitation robotics*, Kyoto, Japan, 23–26 June 2009, pp. 761–765. IEEE.
- Sarakoglou I, Tzagarakis NG and Caldwell DG (2004) Occupational and physical therapy using a hand exoskeleton based exerciser. In: *17th IEEE/RSJ international conference on intelligent robots and systems*, Sendai, Japan, 28 September–2 October 2004, vol. 3, pp. 2973–2978. IEEE.
- Schabowsky C, Godfrey S, Holley R and Lum P (2010) Development and pilot testing of HEXORR: Hand exoskeleton rehabilitation robot. *Journal of NeuroEngineering and Rehabilitation* 7(1): 1–16.
- Schmidt RA and Bjork RA (1992) New conceptualizations of practice: Common principles in three paradigms suggest new concepts for training. *Psychological Science* 3(4): 207–217.
- Sergi F, Lee MM and O'Malley MK (2013) Design of a series elastic actuator for a compliant parallel wrist rehabilitation robot. *IEEE international conference on rehabilitation robotics*, Seattle, WA, USA, 24–26 June 2013, pp. 1–6. IEEE.
- Sheridan T and Ferrell W (1974) *Man–Machine Systems: Introductory Control and Decision Models of Human Performance*. Cambridge, MA: MIT Press.
- Slotine J and Sastry SS (1983) Tracking control of non-linear systems using sliding surfaces, with application to robot manipulators. *International Journal of Control* 38(2): 465–492.
- Smith SW (2003) *Digital Signal Processing: A Practical Guide for Engineers and Scientists*. Boston, MA: Newnes.
- Taheri H, Rowe JB, Gardner D, Chan V, Gray K, Bower C, Reinkensmeyer DJ and Wolbrecht ET (2014) Design and preliminary evaluation of the finger rehabilitation robot: controlling challenge and quantifying finger individuation during musical computer game play. *Journal of Neuroengineering and Rehabilitation* 11(1): 10.
- Takagi M, Iwata K, Takahashi Y, Yamamoto SI, Koyama H and Komeda T (2009) Development of a grip aid system using air cylinders. In: *2009 IEEE international conference on robotics and automation*, Kobe, Japan, 12–17 May 2009, pp. 2312–2317. IEEE.
- Takahashi CD, Der-Yeghiaian L, Le V, Motiwala RR and Cramer SC (2008) Robot-based hand motor therapy after stroke. *Brain* 131(2): 425–437.
- Tong K, Ho S, Pang P, Hu X, Tam W, Fung K, Wei X, Chen P and Chen M (2010) An intention driven hand functions task training robotic system. In: *Annual international conference of the IEEE engineering in medicine and biology society*, Buenos Aires, Argentina, 1–4 September 2010, pp. 3406–3409. IEEE.
- Toya K, Miyagawa T, Kubota Y (2011) Power-assist glove operated by predicting the grasping mode. *Journal of System Design and Dynamics* 5(1): 94–108.
- Ueki S, Kawasaki H, Ito S, Nishimoto Y, Abe M, Aoki T, Ishigure Y, Ojika T and Mouri T (2012) Development of a hand-assist robot with multi-degrees-of-freedom for rehabilitation therapy. *IEEE/ASME Transactions on Mechatronics* 17(1): 136–146.
- Vallery H, Veneman J, Van Asseldonk E, Ekkelenkamp R, Buss M and Van Der Kooij H (2008) Compliant actuation of rehabilitation robots. *IEEE Robotics & Automation Magazine* 15(3): 60–69.
- Vallery H, Duschau-Wicke A and Riener R (2009) Optimized passive dynamics improve transparency of haptic devices. In: *2009 IEEE international conference on robotics and automation*, Kobe, Japan, 12–17 May 2009, pp. 301–306. IEEE.
- Veneman JF, Ekkelenkamp R, Kruidhof R, van der Helm FC and van der Kooij H (2006) A series elastic-and bowden-cable-based actuation system for use as torque actuator in exoskeleton-type robots. *The International Journal of Robotics Research* 25(3): 261–281.
- Wang S, Li J, Zheng R, Chen Z and Zhang Y (2011) Multiple rehabilitation motion control for hand with an exoskeleton. In: *2011 IEEE international conference on robotics and automation*, Shanghai, China, 9–13 May 2011, pp. 3676–3681. IEEE.
- Wege A and Hommel G (2005) Development and control of a hand exoskeleton for rehabilitation of hand injuries. In: *5th IEEE/RSJ international conference on intelligent robots and systems*, Raleigh, NC, 2–6 August 2005, pp. 3046–3051. IEEE.
- Wege A, Kondak K and Hommel G (2006) Force control strategy for a hand exoskeleton based on sliding mode position control. In: *19th IEEE/RSJ international conference on intelligent*

robots and systems, Beijing, China, 9–15 October 2006, pp. 4615–4620. IEEE.

Wu JZ, An KN, Cutlip RG, Krajnak K, Welcome D and Dong RG (2008) Analysis of musculoskeletal loading in an index finger during tapping. *Journal of Biomechanics* 41(3): 668–676.

Zhou J, Malric F and Shirmohammadi S (2010) A new hand-measurement method to simplify calibration in cyberglove-based virtual rehabilitation. *IEEE Transactions on Instrumentation and Measurement* 59(10): 2496–2504.

Appendix: Expression for Jacobian

The expression for Jacobian ($\mathbf{J} = \frac{\partial \mathbf{X}}{\partial \Theta_r}$) is obtained symbolically using MATLAB as expressed in (19).

$$\begin{aligned}
 J_{1,1} &= \frac{l_{BC} l_{CD} \cos(\theta_1 - \theta_4)}{x_3} - l_{BC} \sin(\theta_1 - \theta_4) \\
 J_{1,2} &= 0 \\
 J_{2,1} &= \frac{l_{BC} \cos(\theta_1 - \theta_4)}{x_3} \\
 J_{2,2} &= 0 \\
 J_{3,1} &= \frac{n_{3,1}}{d_{3,1}} \\
 J_{3,2} &= -\frac{l_{EF} \cos(\theta_{HFG} + \theta_5 - \theta_8 + \theta_{6r})}{l_{EF} \cos(\theta_{HFG} + \theta_5 - \theta_8 + \theta_{6r}) - l_{CE} \cos(\theta_{HFG} + \theta_5 - \theta_8)} \\
 J_{4,1} &= \frac{n_{4,1}}{d_{4,1}} \\
 J_{4,2} &= \frac{l_{CE} l_{EF} \sin(\theta_{6r})}{l_{FH} (l_{EF} \cos(\theta_{HFG} + \theta_5 - \theta_8 + \theta_{6r}) - l_{CE} \cos(\theta_{HFG} + \theta_5 - \theta_8))} \quad (19)
 \end{aligned}$$

where $J_{i,j}$ represents the $(i,j)^{th}$ entry in the Jacobian and

$$\begin{aligned}
 n_{3,1} &= -\frac{5 l_{BC} \sin\left(\theta_{HFG} + \tan^{-1}\left(\frac{l_{AH}-x_3}{l_{CD}}\right) + \theta_1 - \theta_8\right) x_3^2}{4} \\
 &- \frac{l_{BC} \sin\left(\tan^{-1}\left(\frac{l_{AH}-x_3}{l_{CD}}\right) - \theta_{HFG} + \theta_1 + \theta_8\right) x_3^2}{4} \\
 &+ \frac{l_{AH}^2 l_{BC} \sin\left(\theta_{HFG} + \tan^{-1}\left(\frac{l_{AH}-x_3}{l_{CD}}\right) - \theta_1 + 2\theta_4 - \theta_8\right)}{2} \\
 &+ \frac{l_{BC} \sin\left(\theta_{HFG} + \tan^{-1}\left(\frac{l_{AH}-x_3}{l_{CD}}\right) - \theta_1 - \theta_8\right) x_3^2}{4} \\
 &+ \frac{l_{BC} \sin\left(\tan^{-1}\left(\frac{l_{AH}-x_3}{l_{CD}}\right) - \theta_{HFG} - \theta_1 + \theta_8\right) x_3^2}{4} \\
 &+ \frac{l_{AH}^2 l_{BC} \sin\left(\theta_{HFG} + \tan^{-1}\left(\frac{l_{AH}-x_3}{l_{CD}}\right) + \theta_1 - \theta_8\right)}{2} \\
 &- \frac{l_{BC} \sin\left(\theta_{HFG} + \tan^{-1}\left(\frac{l_{AH}-x_3}{l_{CD}}\right) - \theta_1 + 2\theta_4 - \theta_8\right) x_3^2}{2}
 \end{aligned}$$

$$\begin{aligned}
 &- \frac{11 l_{BC} l_{CD} \cos\left(\theta_{HFG} + \tan^{-1}\left(\frac{l_{AH}-x_3}{l_{CD}}\right) + \theta_1 - \theta_8\right) x_3}{8} \\
 &- \frac{l_{BC} l_{CD} \cos\left(\tan^{-1}\left(\frac{l_{AH}-x_3}{l_{CD}}\right) - \theta_{HFG} + \theta_1 + \theta_8\right) x_3}{8} \\
 &- \frac{7 l_{AH} l_{BC} \sin\left(\theta_{HFG} + \tan^{-1}\left(\frac{l_{AH}-x_3}{l_{CD}}\right) + \theta_1 - \theta_8\right) x_3}{4} \\
 &+ \frac{l_{AH} l_{BC} \sin\left(\tan^{-1}\left(\frac{l_{AH}-x_3}{l_{CD}}\right) - \theta_{HFG} + \theta_1 + \theta_8\right) x_3}{4} \\
 &+ l_{AH} l_{BC} l_{CD} \cos\left(\theta_{HFG} + \tan^{-1}\left(\frac{l_{AH} - x_3}{l_{CD}}\right) - \theta_1 + 2\theta_4 - \theta_8\right) \\
 &- \frac{l_{BC} l_{CD} \cos\left(\theta_{HFG} + \tan^{-1}\left(\frac{l_{AH}-x_3}{l_{CD}}\right) - \theta_1 - \theta_8\right) x_3}{8} \\
 &+ \frac{l_{BC} l_{CD} \cos\left(\tan^{-1}\left(\frac{l_{AH}-x_3}{l_{CD}}\right) - \theta_{HFG} - \theta_1 + \theta_8\right) x_3}{8} \\
 &- \frac{l_{AH} l_{BC} \sin\left(\theta_{HFG} + \tan^{-1}\left(\frac{l_{AH}-x_3}{l_{CD}}\right) - \theta_1 - \theta_8\right) x_3}{4} \\
 &- \frac{l_{AH} l_{BC} \sin\left(\tan^{-1}\left(\frac{l_{AH}-x_3}{l_{CD}}\right) - \theta_{HFG} - \theta_1 + \theta_8\right) x_3}{4} \\
 &+ l_{AH} l_{BC} l_{CD} \cos\left(\theta_{HFG} + \tan^{-1}\left(\frac{l_{AH} - x_3}{l_{CD}}\right) + \theta_1 - \theta_8\right) \\
 &- \frac{l_{BC} l_{CD} \cos\left(\theta_{HFG} + \tan^{-1}\left(\frac{l_{AH}-x_3}{l_{CD}}\right) - \theta_1 + 2\theta_4 - \theta_8\right) x_3}{2} \\
 &+ \frac{l_{BC} \sin(\theta_{HFG} + \theta_1 - \theta_8) x_3^2}{2\sqrt{\frac{(l_{AH}-x_3)^2}{l_{CD}^2} + 1}} \\
 &+ \frac{l_{BC} \sin(\theta_1 - \theta_{HFG} + \theta_8) x_3^2}{2\sqrt{\frac{(l_{AH}-x_3)^2}{l_{CD}^2} + 1}} \\
 &- \frac{l_{BC} l_{CD} \cos(\theta_{HFG} + \theta_1 - \theta_8) x_3}{4\sqrt{\frac{(l_{AH}-x_3)^2}{l_{CD}^2} + 1}} \\
 &+ \frac{l_{BC} l_{CD} \cos(\theta_1 - \theta_{HFG} + \theta_8) x_3}{4\sqrt{\frac{(l_{AH}-x_3)^2}{l_{CD}^2} + 1}} \\
 &- \frac{l_{AH} l_{BC} \sin(\theta_{HFG} + \theta_1 - \theta_8) x_3}{2\sqrt{\frac{(l_{AH}-x_3)^2}{l_{CD}^2} + 1}} \\
 &- \frac{l_{AH} l_{BC} \sin(\theta_1 - \theta_{HFG} + \theta_8) x_3}{2\sqrt{\frac{(l_{AH}-x_3)^2}{l_{CD}^2} + 1}} \\
 d_{3,1} &= x_3 (l_{EF} \cos(\theta_{HFG} + \theta_5 - \theta_8 + \theta_{6r}) - l_{CE} \cos(\theta_{HFG} + \theta_5 - \theta_8))
 \end{aligned}$$

$$\begin{aligned}
 n_{4,1} = & \frac{l_{BC} l_{CE} \cos\left(\tan^{-1}\left(\frac{l_{AH}-x_3}{l_{CD}}\right) - \theta_1 + \theta_5\right) x_3^2}{4} \\
 & - \frac{l_{BC} l_{EF} \cos\left(\tan^{-1}\left(\frac{l_{AH}-x_3}{l_{CD}}\right) - \theta_1 + 2\theta_4 - \theta_5 - \theta_{6r}\right) x_3^2}{2} \\
 & + \frac{5 l_{BC} l_{CE} \cos\left(\tan^{-1}\left(\frac{l_{AH}-x_3}{l_{CD}}\right) + \theta_1 - \theta_5\right) x_3^2}{4} \\
 & - \frac{l_{BC} l_{EF} \cos\left(\tan^{-1}\left(\frac{l_{AH}-x_3}{l_{CD}}\right) - \theta_1 + \theta_5 + \theta_{6r}\right) x_3^2}{4} \\
 & - \frac{l_{AH}^2 l_{BC} l_{CE} \cos\left(\tan^{-1}\left(\frac{l_{AH}-x_3}{l_{CD}}\right) - \theta_1 + 2\theta_4 - \theta_5\right)}{2} \\
 & + \frac{5 l_{BC} l_{EF} \cos\left(\tan^{-1}\left(\frac{l_{AH}-x_3}{l_{CD}}\right) + \theta_1 - \theta_5 - \theta_{6r}\right) x_3^2}{4} \\
 & - \frac{l_{BC} l_{CE} x_3^2 \cos\left(\tan^{-1}\left(\frac{l_{AH}-x_3}{l_{CD}}\right) - \theta_1 - \theta_5\right)}{4} \\
 & + \frac{l_{AH}^2 l_{BC} l_{EF} \cos\left(\tan^{-1}\left(\frac{l_{AH}-x_3}{l_{CD}}\right) - \theta_1 + 2\theta_4 - \theta_5 - \theta_{6r}\right)}{2} \\
 & - \frac{l_{AH}^2 l_{BC} l_{CE} \cos\left(\tan^{-1}\left(\frac{l_{AH}-x_3}{l_{CD}}\right) + \theta_1 - \theta_5\right)}{2} \\
 & + \frac{l_{BC} l_{EF} \cos\left(\tan^{-1}\left(\frac{l_{AH}-x_3}{l_{CD}}\right) + \theta_1 + \theta_5 + \theta_{6r}\right) x_3^2}{4} \\
 & - \frac{l_{BC} l_{CE} \cos\left(\tan^{-1}\left(\frac{l_{AH}-x_3}{l_{CD}}\right) + \theta_1 + \theta_5\right) x_3^2}{4} \\
 & + \frac{l_{BC} l_{CE} \cos\left(\tan^{-1}\left(\frac{l_{AH}-x_3}{l_{CD}}\right) - \theta_1 + 2\theta_4 - \theta_5\right) x_3^2}{2} \\
 & + \frac{l_{BC} l_{EF} \cos\left(\tan^{-1}\left(\frac{l_{AH}-x_3}{l_{CD}}\right) - \theta_1 - \theta_5 - \theta_{6r}\right) x_3^2}{4} \\
 & + \frac{l_{AH}^2 l_{BC} l_{EF} \cos\left(\tan^{-1}\left(\frac{l_{AH}-x_3}{l_{CD}}\right) + \theta_1 - \theta_5 - \theta_{6r}\right)}{2} \\
 & + \frac{l_{AH} l_{BC} l_{EF} \cos\left(\tan^{-1}\left(\frac{l_{AH}-x_3}{l_{CD}}\right) - \theta_1 + \theta_5 + \theta_{6r}\right) x_3}{4} \\
 & + \frac{l_{BC} l_{EF} \cos(\theta_1 - \theta_5 - \theta_{6r}) x_3^2}{2\sqrt{\frac{(l_{AH}-x_3)^2}{l_{CD}^2} + 1}} \\
 & + \frac{l_{BC} l_{CD} l_{EF} \sin\left(\tan^{-1}\left(\frac{l_{AH}-x_3}{l_{CD}}\right) - \theta_1 + \theta_5 + \theta_{6r}\right) x_3}{8} \\
 & + \frac{l_{BC} l_{CD} l_{EF} \sin\left(\tan^{-1}\left(\frac{l_{AH}-x_3}{l_{CD}}\right) - \theta_1 + 2\theta_4 - \theta_5 - \theta_{6r}\right) x_3}{2} \\
 & + \frac{7 l_{AH} l_{BC} l_{CE} \cos\left(\tan^{-1}\left(\frac{l_{AH}-x_3}{l_{CD}}\right) + \theta_1 - \theta_5\right) x_3}{4} \\
 & - \frac{l_{AH} l_{BC} l_{CE} \cos\left(\tan^{-1}\left(\frac{l_{AH}-x_3}{l_{CD}}\right) - \theta_1 + \theta_5\right) x_3}{4} \\
 & - \frac{3 l_{BC} l_{CD} l_{CE} \sin\left(\tan^{-1}\left(\frac{l_{AH}-x_3}{l_{CD}}\right) + \theta_1 - \theta_5\right) x_3}{2} \\
 & + \frac{l_{AH} l_{BC} l_{CD} l_{CE} \sin\left(\tan^{-1}\left(\frac{l_{AH}-x_3}{l_{CD}}\right) - \theta_1 + 2\theta_4 - \theta_5\right)}{2} \\
 & - \frac{l_{BC} l_{EF} \cos(\theta_1 + \theta_5 + \theta_{6r}) x_3^2}{2\sqrt{\frac{(l_{AH}-x_3)^2}{l_{CD}^2} + 1}} \\
 & - \frac{7 l_{AH} l_{BC} l_{EF} \cos\left(\tan^{-1}\left(\frac{l_{AH}-x_3}{l_{CD}}\right) + \theta_1 - \theta_5 - \theta_{6r}\right) x_3}{4} \\
 & + \frac{l_{BC} l_{CE} \cos(\theta_1 + \theta_5) x_3^2}{2\sqrt{\frac{(l_{AH}-x_3)^2}{l_{CD}^2} + 1}} \\
 & + \frac{11 l_{BC} l_{CD} l_{EF} x_3 \sin\left(\tan^{-1}\left(\frac{l_{AH}-x_3}{l_{CD}}\right) + \theta_1 - \theta_5 - \theta_{6r}\right)}{8} \\
 & + \frac{l_{AH} l_{BC} l_{CE} x_3 \cos\left(\tan^{-1}\left(\frac{l_{AH}-x_3}{l_{CD}}\right) - \theta_1 - \theta_5\right)}{4} \\
 & - l_{AH} l_{BC} l_{CD} l_{EF} \sin\left(\tan^{-1}\left(\frac{l_{AH}-x_3}{l_{CD}}\right) - \theta_1 + 2\theta_4 - \theta_5 - \theta_{6r}\right) \\
 & - \frac{l_{AH} l_{BC} l_{EF} \cos\left(\tan^{-1}\left(\frac{l_{AH}-x_3}{l_{CD}}\right) + \theta_1 + \theta_5 + \theta_{6r}\right) x_3}{4} \\
 & + \frac{l_{AH} l_{BC} l_{CD} l_{CE} \sin\left(\tan^{-1}\left(\frac{l_{AH}-x_3}{l_{CD}}\right) + \theta_1 - \theta_5\right)}{4} \\
 & - \frac{l_{BC} l_{CD} l_{EF} \sin\left(\tan^{-1}\left(\frac{l_{AH}-x_3}{l_{CD}}\right) + \theta_1 + \theta_5 + \theta_{6r}\right) x_3}{8} \\
 & + \frac{l_{AH} l_{BC} l_{CE} \cos\left(\tan^{-1}\left(\frac{l_{AH}-x_3}{l_{CD}}\right) + \theta_1 + \theta_5\right) x_3}{4} \\
 & - \frac{l_{AH} l_{BC} l_{EF} \cos\left(\tan^{-1}\left(\frac{l_{AH}-x_3}{l_{CD}}\right) - \theta_1 - \theta_5 - \theta_{6r}\right) x_3}{4} \\
 & - \frac{l_{BC} l_{CE} x_3^2 \cos(\theta_1 - \theta_5)}{2\sqrt{\frac{(l_{AH}-x_3)^2}{l_{CD}^2} + 1}} \\
 & - \frac{l_{BC} l_{CD} l_{CE} \sin\left(\tan^{-1}\left(\frac{l_{AH}-x_3}{l_{CD}}\right) - \theta_1 + 2\theta_4 - \theta_5\right) x_3}{2} \\
 & + \frac{l_{BC} l_{CD} l_{EF} \sin\left(\tan^{-1}\left(\frac{l_{AH}-x_3}{l_{CD}}\right) - \theta_1 - \theta_5 - \theta_{6r}\right) x_3}{8} \\
 & + \frac{l_{AH} l_{BC} l_{CD} l_{EF} \sin\left(\tan^{-1}\left(\frac{l_{AH}-x_3}{l_{CD}}\right) + \theta_1 - \theta_5 - \theta_{6r}\right)}{2} \\
 & - \frac{l_{AH} l_{BC} l_{EF} \cos(\theta_1 - \theta_5 - \theta_{6r}) x_3}{2\sqrt{\frac{(l_{AH}-x_3)^2}{l_{CD}^2} + 1}} \\
 & + \frac{l_{BC} l_{CD} l_{EF} \sin(\theta_1 - \theta_5 - \theta_{6r}) x_3}{4\sqrt{\frac{(l_{AH}-x_3)^2}{l_{CD}^2} + 1}}
 \end{aligned}$$

$$\begin{aligned}
& + \frac{l_{AH} l_{BC} l_{EF} \cos(\theta_1 + \theta_5 + \theta_{6r}) x_3}{2 \sqrt{\frac{(l_{AH} - x_3)^2}{l_{CD}^2} + 1}} \\
& + \frac{l_{BC} l_{CD} l_{EF} \sin(\theta_1 + \theta_5 + \theta_{6r}) x_3}{4 \sqrt{\frac{(l_{AH} - x_3)^2}{l_{CD}^2} + 1}} \\
& - \frac{l_{AH} l_{BC} l_{CE} \cos(\theta_1 + \theta_5) x_3}{2 \sqrt{\frac{(l_{AH} - x_3)^2}{l_{CD}^2} + 1}}
\end{aligned}$$

$$+ \frac{l_{AH} l_{BC} l_{CE} x_3 \cos(\theta_1 - \theta_5)}{2 \sqrt{\frac{(l_{AH} - x_3)^2}{l_{CD}^2} + 1}}$$

$$\begin{aligned}
d_{4,1} &= l_{FH} x_3 (l_{EF} \cos(\theta_{HFG} + \theta_5 - \theta_8 + \theta_{6r}) \\
&\quad - l_{CE} \cos(\theta_{HFG} + \theta_5 - \theta_8))
\end{aligned}$$

The derivative of the Jacobian is evaluated numerically using (20).

$$\dot{\mathbf{J}}(t) = \frac{\mathbf{J}(t) - \mathbf{J}(t - \Delta t)}{\Delta t} \quad (20)$$